Utrecht University

Bachelor Thesis
Faculteit Bètawetenschappen
Natuur- en Sterrenkunde

Minimal model of a nodal cilium

Hydrodynamic flow patterns and synchronization of two interacting cilia

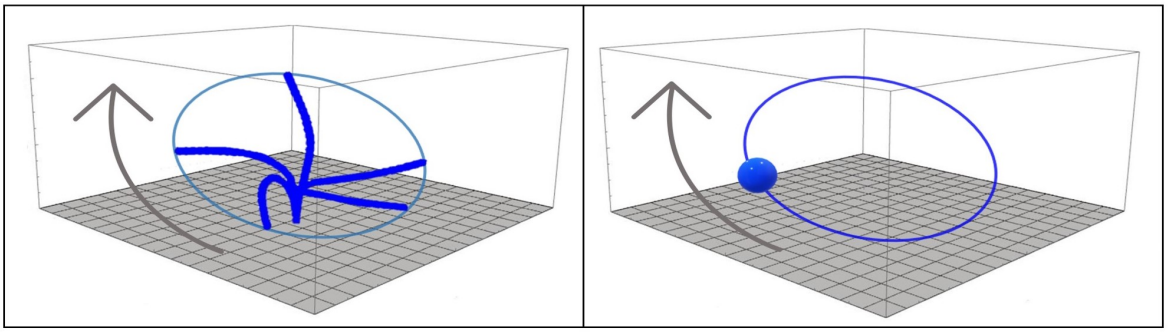

Author:
Bo van den Bosch
(5718791)

Supervised by:
Dr. Joost de Graaf
Institute for Theoretical Physics

June 26, 2020

Abstract

The human body is nearly left-right symmetric on the outside, but this is not the case on the inside. During the development of the body, a leftward fluid movement in the node (a cavity that will turn into the embryo) is essential for the left-right symmetry-breaking process. However, the exact role of nodal flow and the hair-like appendages (cilia) that produce this is still debated. In this thesis we study a minimal model of a nodal cilium with only one degree of freedom. In this model, originally proposed by Vilfan and Jülicher, Phys. Rev. Lett. **96**, 058102 (2006), a cilium is replaced by a spherical bead moving on a fixed elliptic orbit. The model cilia interact hydrodynamically which allows for the study of synchronization. In this thesis we compare the minimal model to an advanced model developed concurrently in another Bachelor project by Perugachi Israels. Surprisingly, we find that the minimal model semi-quantitatively captures the features and generates fluid dynamics comparable to the advanced model. Consequently, the minimal model can be used to qualitatively study processes like the flow-induced movement of small signaling molecules. Duplicating the minimal model allows us to study synchronization between neighboring cilia. Doing so, we notice that the model cannot take into account the change in the trajectory of a cilium due to the presence of a second cilium. This problem can be solved by adding another degree of freedom to the minimal model, which is left for future study.

Description of the cover image: A visualization of the minimal model originally proposed by Vilfan and Jülicher [1]. Figure on the left: Model cilium by Perugachi Israels [2]. The tip of a cilium describes a elliptic orbit. The cilium is replaced by a spherical bead moving on this elliptic trajectory (figure on the right).

Contents

1 Introduction

There are several aspects of the human body that display symmetry. This includes, for example, physical appearance and the placement of the kidneys. However, this is not the case in on the inside. Some organs are placed in an asymmetric manner, *e.g.* the heart is positioned on the left and liver towards the right. In the human body, a three dimensional object, we distinguish between three axes: front-back, up-down, and left-right [3]. Accurate positioning of the organs during embryonic development requires the left-right axis to be correctly established. A mistake in establishing this axis can lead to random positioning (heterotaxy/situs ambiguous) or a completely reverse positioning (situs inversus totalis) of the organs [4].

The formation of the body starts from an oocyte, which is a symmetrical round shaped egg. Subsequently, an embryonic cavity is formed, called the node. The embryo is completely symmetric during this period. Breaking down this symmetry is crucial in the process of developing the human body [3, 4]. The research conducted during the last decade shows that leftward fluid movement in the node is essential in the left-right symmetry-breaking process [3]. For instance, Okada *et al.* (1999) showed that defects in organ positioning are always accompanied by abnormalities in nodal flow [5].

Nodal flow is generated by the tilted rotational motion of cilia, which are vibrating hair-like microscopic structures attached to the surface of certain cells, including cells in the node [6, 7]. The central role cilia play in the left-right symmetry-breaking process is shown in numerous experiments. For instance, a study by Okada *et al.* (1999) demonstrates that mouse mutants with immotile nodal cilia, which leads to an absent nodal flow, exhibited randomized positioning of the organs along the left-right axis [5]. In a different research by Shinohara *et al.* (2012) embryos with only one motile cilium are studied. In these embryos left-right asymmetry is never observed, regardless of the position of the cilium in the node [6]. A study by Nonaka *et al.* (2002) demonstrates that mice with an artificially induced rightward flow show inverted organ placement [8]. These experiments greatly contribute to the consensus that nodal cilia play an important role in establishing correct organ positioning. However, how nodal fluid flow exactly leads to asymmetric organ positioning is still debated.

Until recently it was believed that rotation of numerous cilia was necessary to establish left-right asymmetry. One of the reasons for this is the observation that a system of in-phase beating cilia can form a wave in the opposite direction of their effective beat, called an antiplectic metachronal wave. This phenomenon leads to a more efficient flow [9, 10, 11]. Experiments indicate that hydrodynamic coupling between cilia could be the cause of the observed metachronal waves [12, 13]. This understanding has been verified in simple systems of artificially coupled cilia with only a few degrees of freedom [1, 14]. These models have shown that hydrodynamic interactions alone can indeed synchronize a system of two simple oscillators.

Counter to the idea that many cilia are required, a recent study by Shinohara (2012) reveales that the leftward flow generated by a system of only two rotating cilia is sufficient to initiate left-right asymmetric gene expression. Left-right asymmetry is already observed a few hours after a system of two cilia start their beating pattern [6]. This has led to further debate on the nature and origin of the left-right asymmetry.

In this thesis we contribute to research on this topic by studying a minimal model of a cilium. The goal is to discover whether a minimal model of a cilium properly captures the features and generates fluid dynamics comparable to that of an advanced model of a cilium. Consequently, we can determine if the minimal model is sufficiently accurate to study processes in the node like the flow-induced movement of small signaling molecules. Studying this process, and other nodal processes may contribute to one of the hypotheses about how nodal flow exactly leads to asymmetric gene expression.

In order to investigate this a cilium will be modeled as a spherical bead moving on a fixed elliptic orbit. This model is originally proposed by Vilfan and Jülicher [1]. The only degree of freedom in this minimal model is the position of the bead along the trajectory, which allows us to study synchronization. The model takes into account the effect of the nearby cell surface on the flow via the Blake tensor. Duplicating this minimal model allows us to study synchronization in a system of two cilia. The influence the neighbouring cilia have on each other will be taken into account using Faxen's Law. In order to answer the research question we compare the minimal model to a more advanced model analyzed by Perugachi Israels [2]. Her model provides a detailed description of a cilium where not only one bead is modeled, but the full shape of a cilium using multiple beads connected by springs. We compare the generated fluid velocity and traction forces (a measure for the internal friction inside the fluid) of the minimal model to the advanced model. Surprisingly, we find that the minimal model semi-quantitatively captures the fluid velocity and other properties of the advanced model. Therefore, the minimal model can be used to qualitatively study nodal processes like the flow-induced movement of small signaling molecules. Studying these nodal processes may contribute to one of the hypotheses (see section 2) about how nodal flow exactly lead to asymmetric gen expression. Duplicating the minimal model has allowed us to study synchronization between neighboring cilia. We observe that the minimal model is highly sensitive to changes in the trajectory of the beads. We notice that a change in trajectory of a cilium due to the presence of a second cilium cannot be taken into account. In order to solve this problem another degree of freedom should be added to the minimal model.

In section 2 we will continue to provide more background information on nodal cilia. Next in section 3, we present the theoretical background needed to describe the fluid flow and traction forces in the node. Subsequently, in section 4 we explain the minimal model in more depth and illustrate how we compare it to the advanced model. Finally, in section 5, 6 and 7 we outline and discuss the results.

2 Biological background information of nodal cilia

Motile cilia are found on the surface of certain cells, where they either cause fluid flow in the surrounding fluid or in small organisms provide, propulsion [15, 16]. There are at least eight categories of cilia in the human body, which play important roles in numerous processes. For example, cilia are involved in clearing the respiratory system, transporting of cerebrospinal fluid, reproductive processes and embryonic development [17]. In this thesis we focus on the role cilia play in embryonic development, specifically in the right-left-symmetry breaking process. The proposed model in this thesis is based on mice nodal cilia.

Motile cilia are active and move with a beating pattern that is generated by motor proteins [18]. In mice embryo, nodal cilia emerge 7.5 days after fertilization in a triangular shaped cavity called the node. The width of the node is approximately 100 μm [3, 17]. Mice nodal cilia are relatively short, about 5 μm, and have a diameter of approximately 150 nm [17, 19]. To each cell of the node only one cilium is attached, this result in an inter-cilia spacing of the order of several cilium lengths [20]. In total, the node contains up to 200-300 cilia [6].

A typical cilium trajectory can be divided into an effective stroke and recovery stroke. During the effective stroke the curved cilium extends and moves rapidly away from the cell surface. Throughout the recovery stroke the bend returns and the cilium moves slowly in a trajectory closer to the cell surface [19, 21]. The beating pattern of nodal cilia differs from this as they exhibit a tilted rotational motion rather than an asymmetric shaped power-and recovery stroke [20]. Mice nodal cilia are tilted $40^\circ \pm 10^\circ$ with respect to the cell surface and rotate clockwise with a frequency of 10 Hz [7]. When the cilium approaches the cell wall closely (during the rightward recovery stroke) it interacts with the nearby boundary. Consequently, the flow in this part of the trajectory is limited and a leftward fluid flow is generated [20, 22]. The nodal flow is approximately $3\,\mu\text{m s}^{-1}$ and is observed $\sim 5\,\mu$m above the cell surface [7]. The leftward flow proceeds to go upward along the left sidewall of the node, following the top membrane of the node called the Reichert's membrane. The flow eventually returns on the right side ($\sim 20\,\mu$m above the cell surface) as a slower counter-flow of approximately $1\,\mu\text{m s}^{-1}$ [7, 23].

The exact role of nodal flow in the symmetry-breaking process is debated. It is believed that nodal flow carries signaling molecules to the left edge of the node where they initiate an asymmetric gene expression pathway [3]. However, this theory has not proven yet and there are a myriad of hypotheses. Another theory argues that immotile cilia on the left side of the node detect the flow directly [24, 25]. To gain insight into the symmetry-breaking process it is essential to study the strength, amount and direction of the nodal flow. Multiple factors can influence the generated nodal flow.

When a system of multiple cilia starts beating, metachronal coordination occurs (neighbouring cilia exhibit a constant phase difference). It is believed that this is a result of the hydrodynamic coupling between the cilia [9, 10, 11]. The degree in which the cilia synchronize greatly affects their ability to transport materials inside the node. In a completely unsynchronized system no materials are transported, independent of all other cilia activity [26].

In order to study these ciliated systems not only experimental research is conducted, but also numerous mathematical models are developed. For example, Smith *et al.* (2011) developed a method to model the effect of the Reichert's membrane on the nodal flow [23]. The computations confirm that the presence of this membrane induces a counter flow as observed in biological reality . Vilfan and Jülicher (2006) propose a different model [1]. This minimal model only exhibits one degree of freedom and therefore allows them to study hydrodynamic interaction between two cilia.

3 Theoretical framework

Nodal (motile) cilia produce fluid flow in the embryonic node. We can describe this flow using the Navier-Stokes equations, which we introduce in this section. For the hydrodynamic regime we are interested in the Navier–Stokes equations reduce to their linearized form, often referred to as the Stokes equations. We continue by stating the fundamental solutions to the Stokes equations and use these to describe the bulk and boundary fluid flow. Using Faxén's law we show that flow can generate the movement of a small sphere that is placed inside the fluid. This allows us to construct a minimal model (originally proposed by Vilfan and Jülicher) where a cilium is represented by a small sphere.

3.1 Equations of motion for a fluid

Cilia move in an incompressible aqueous fluid and consequently generate fluid flow. We describe the flow using the Navier-Stokes equations, which govern mass and momentum transport from conservation laws. The Navier-Stokes equations are stated below. We respectively have the incompressibility equation (equation 1), conservation of mass (equation 2) and conservation of momentum (equation 3) [27].

$$\nabla_{\mathbf{r}} \cdot \mathbf{u}(\mathbf{r}, t) = 0 \tag{1}$$

$$\frac{D}{Dt}\rho(\mathbf{r}, t) = 0 \tag{2}$$

$$\rho(\mathbf{r}, t)\frac{D}{Dt}\mathbf{u}(\mathbf{r}, t) = -\nabla_{\mathbf{r}} p(\mathbf{r}, t) + \mu \boldsymbol{\Delta}_{\mathbf{r}} \mathbf{u}(\mathbf{r}, t) + \mathbf{f}(\mathbf{r}, t) \tag{3}$$

In these equations:

- $\mathbf{u}(\mathbf{r}, t)$ is the velocity
- $\rho(\mathbf{r}, t)$ is the density
- $\mathbf{f}(\mathbf{r}, t)$ is the external force applied on the fluid
- $\mathbf{p}(\mathbf{r}, t)$ is the pressure
- μ is the viscosity
- $\dfrac{D}{Dt} = \dfrac{\partial}{\partial t} + \mathbf{u}(\mathbf{r}, t) \cdot \boldsymbol{\nabla}_{\boldsymbol{r}}$ is the material derivative

Note that we choose to ignore the energy transport equation. We are allowed to do this if there are no significant temperature gradients. We assume this is the case in our ciliated system. This is a reasonable assumption for two main reasons: First, there are no significant external temperature gradients in the embryonic cavity. Therefore, the system is considered isothermal, meaning no heat is transferred in or out of our system. Secondly, we study a system at small length scales. This means that viscous dissipation (the heating of the fluid due to internal friction) does not lead to significant local heating. Using the above we can justify ignoring the energy transport equation [28].

3.2 Stress in a fluid

In order to study the influence of a beating cilium on the surrounding substrate we need a measure for the internal forces in the fluid. These can be expressed in terms of a three-dimensional matrix called the stress tensor. The forces that act inside the fluid result in a displacement of a volume element which we can express in terms of a second tensor called the strain tensor [29]. We will now quantify the Stress and Strain tensor and describe a relation between the two. We start our discussion at the momentum transport equation in a slightly different form than previously stated in equation 3 [28]:

$$\rho(\boldsymbol{r},t)\frac{D}{Dt}\boldsymbol{u}(\boldsymbol{r},t) = \boldsymbol{\nabla}_{\boldsymbol{r}} \cdot \underline{\boldsymbol{\sigma}}(\boldsymbol{r},t) + \boldsymbol{f}(\boldsymbol{r},t), \tag{4}$$

Here $\underline{\boldsymbol{\sigma}}(\boldsymbol{r},t)$ denotes the stress tensor. By specifying the stress tensor we can capture the behaviour of numerous suspensions [28]. The stress tensor relates a force $\mathbf{F}$ acting on a surface element dA in a linear fashion [29]:

$$F_i(d\mathbf{A}) = \sum_{j=1}^{3} \sigma_{ij} dA_j \tag{5}$$

The off-diagonal elements of the stress tensor σ_{ij} $(i \neq j)$ contain shear stresses which give information about the deformation of a fluid element[1]. We will denote the shear elements of the stress tensor as τ. The diagonal elements of the stress tensor σ_{ii} $(i = j)$ contain the normal components of the force per area on the surface of a fluid element. The normal stresses give information about the volume change of a fluid element[2]. When a fluid is subjected to hydrostatic pressure only we can relate the change in volume directly to the change in pressure [28, 29]. We use this to rewrite the stress tensor for a fluid by isolating the shear stresses from the normal stresses:

$$\underline{\boldsymbol{\sigma}}(\mathbf{r},t) = -p(\mathbf{r},t)\mathbb{I}_3 + \underline{\boldsymbol{\tau}}(\mathbf{r},t), \tag{6}$$

where $p(\mathbf{r},t)$ is the pressure (containing the normal stresses) and $\underline{\boldsymbol{\tau}}(\mathbf{r},t)$ is the deviatoric stress tensor (containing the shear stresses). The stress tensor can be related to the traction forces, which measure the internal friction in the fluid. We define the outward-pointing normal vector of a fluid volume element as $\hat{\boldsymbol{n}}(\boldsymbol{r},t)$. The traction yields:

$$\boldsymbol{T}(\boldsymbol{r},t) = \hat{\boldsymbol{n}}(\boldsymbol{r},t) \cdot \underline{\boldsymbol{\sigma}}(\mathbf{r},t) \tag{7}$$

How a control volume exactly deforms is defined by the strain-rate tensor $\dot{\underline{\boldsymbol{\gamma}}}(\mathbf{r},t)$. The dot denotes that the variation of a control volume over time is considered. The strain rate tensor is defined as [28]:

$$\dot{\underline{\boldsymbol{\gamma}}}(\mathbf{r},t) = \big(\boldsymbol{\nabla}_{\boldsymbol{r}}\mathbf{u}(\mathbf{r},t)\big) + \big(\boldsymbol{\nabla}_{\boldsymbol{r}}\mathbf{u}(\mathbf{r},t)\big)^T, \tag{8}$$

where $\mathbf{u}(\mathbf{r},t)$ is the fluid velocity field. The strain rate tensor is related to the deviatoric stress tensor (which in our case of a fluid only contains shear stress) by the viscosity μ [28]:

$$\underline{\boldsymbol{\tau}}(\mathbf{r},t) = \mu\dot{\underline{\boldsymbol{\gamma}}}(\mathbf{r},t) \tag{9}$$

In this thesis we will report the traction on the surface rather than the entire stress tensor. This quantity is easier to visualize and gives more insight in the results.

[1] Generally the off-diagonal elements of the stress tensor contain shear stresses and other stresses. However, when studying a incompressible Newtonian fluid the off diagonal elements of the stress tensor only contain shear stresses [28].

[2] When considering a fluid the normal stresses are equal [28]

3.3 From Navier–Stokes to Stokes

We examine the the Navier–Stokes equations in more detail and note that there are nonlinear terms in the fluid velocity $\mathbf{u}(\mathbf{r}, t)$ due to the second term on the left-hand side of equation 3. The non-linear terms in fluid velocity make the Navier–Stokes equation difficult to solve. One can estimate the importance of each term through dimensional analysis.

We now introduce dimensionless (accent) quantities by writing: $t = Tt'$, $r = Lr'$, $u = Uu'$, $p = \mu Up'/L$ and $f = \mu Uf'/L^2$. Where T represents the characteristic time of the system, L the length and U the speed. We can write the momentum transport equation (equation 3) in a non-dimensional form using our non-dimensional parameters:

$$\mathrm{Re}(\mathrm{St}\frac{\partial}{\partial t'} + \mathbf{u}' \cdot \nabla')\mathbf{u}' = -\nabla' p + \Delta' u' + f' \tag{10}$$

Here we have introduced the Reynolds number and the Strouhal number respectively:

$$\begin{aligned} \mathrm{Re} &= \frac{\rho \mathrm{UL}}{\mu} \\ \mathrm{St} &= \frac{\mathrm{L}}{\mathrm{UT}} \end{aligned} \tag{11}$$

The Reynolds number is a measure of the importance of inertia (ρUL) relative to viscous effects (μ). The Strouhal number is a measure of the importance of convective transport L/U to perturbations of the flow field T [28].

In case the Reynolds number is high the inertia effects dominate over viscous dissipation. As a result the left-hand side of equation 10, containing the time derivatives and convective transport, dominates over the right-hand side. When the Reynolds number is low, the right-hand side of equation 10, containing the viscous effects, dominates the left-hand side. When $\mathrm{Re} \ll 1$ but the combination $\mathrm{ReSt} \gtrsim 1$, the non linear term in the Navier–Stokes equation becomes irrelevant but the the time derivative does not. On condition that $\mathrm{Re} \ll 1$ and $\mathrm{St} \ll 1$ the right hand side of equation 10 dominates over the left-hand side, i.e. the viscous dissipation dominates over the inertia. Both the non-linear and the time-dependent terms drop out and equation 10 can be approximated by the linear Stokes equation:

$$\mu \boldsymbol{\Delta} \mathbf{u} = \nabla p - \mathbf{f} \tag{12}$$

Here we have reinstated the dimension-full notation. The linearized Stokes equations describe fluid flows that are referred to as laminar.

Reynolds number in ciliated systems
In this thesis we examine a ciliated system in an embryonic node. We work with a fluid that has the density and viscosity of water at 36° [30] (the temperate of mice), hence $\rho = 1.0 \cdot 10^3$ kg m^{-3} and $\mu = 7.0 \cdot 10^{-4}$ Pa. Mice nodal cilia in mice are about 5 μm long [19] and rotate with a approximate frequency of 10 Hz [7]. We use the above parameters to compute the the Reynolds and Strouhal number for our ciliated system and find: $\mathrm{Re} \sim 10^{-4}$ and $\mathrm{St} \sim 10^{-1}$. Therefore the Navier–Stokes equations reduce to the Stokes equations. We repeat the two relevant equations below.

$$\mu \boldsymbol{\Delta} \mathbf{u} = \nabla p - \mathbf{f} \tag{13}$$

$$\nabla \cdot \mathbf{u} = 0 \tag{14}$$

Note that we did not include equation 2, which tells us the density change with respect to time. This is because we are working in a homogeneous incompressible medium rendering equation 2 irrelevant.

3.4 Solving the Stokes equations

Solving equation 13 and 14 reveals the fluid behaviour at the hydrodynamic regime we are interested in. First, we will examine the fluid behavior of the bulk system. We continue studying the fluid behavior near a boundary. Finally, we will provide an expression for the pressure in the fluid near a boundary.

Fluid behavior of the bulk system

The solutions to the stationary Stokes equations are Green's functions, which can be derived by going to Fourier space. For a more detailed description of solving the Stokes equations see reference [31]. The solved Stokes equations are described by the Stokeslet solution. The fluid flow velocity $\mathbf{u}(\mathbf{r})$ at an arbitrary point $\mathbf{r}$ is linearly related to the point force $\mathbf{f}$ which is applied to the fluid at $\mathbf{r}'$ by [31, 32]:

$$\mathbf{u}(\mathbf{r}) = \frac{\mathbf{f}}{8\pi\mu}\mathbf{G}^O(\mathbf{r} - \mathbf{r}') \tag{15}$$

Where $\mathbf{G}^O$ is the Stokeslet, also commonly referred to as the Oseen tensor:

$$\mathbf{G}^O(\mathbf{r}) = \frac{1}{r}\mathbb{I}_3 + \frac{\mathbf{r} \otimes \mathbf{r}}{r^3} \tag{16}$$

Here $\mathbb{I}_3$ is the 3×3 identity matrix and $\otimes$ denotes a dyadic product. The fluid flow velocity $\mathbf{u}(\mathbf{r})$, when a point force $\mathbf{f}$ is applied to the fluid, is visualized in the figure below:

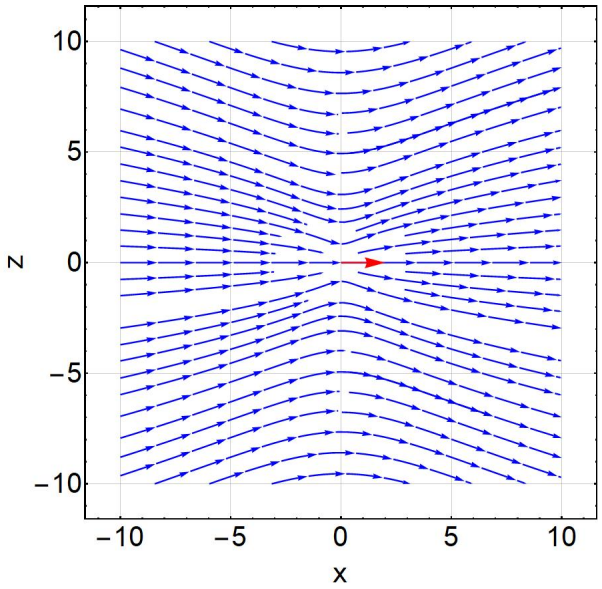

Figure 1: The flow field $\mathbf{u}(\mathbf{r})$ of the Stokeslet solution is represented by the blue streamlines. A point force $\mathbf{f} = (1, 0, 0)$ is applied to the fluid, represented by the red arrow.

Fluid behavior near a boundary

A cilium is attached to a cell surface. Therefore we are interested in fluid behaviour near this boundary. We know that the flow at the boundary has zero velocity relative to the boundary. This phenomena is referred to as the no-slip boundary condition [33]. The point-force solution of the Stokes equations that satisfies the no-slip condition is named the Blake tensor and is derived using the method of images [34, 35].

The method of images is a mathematical tool which allows us to solve differential equations by placing a mirror image in the half-space below the plane of the original image. As a result the no-slip boundary condition is satisfied. You may recall this method form electrostatics. Here, a mirror charge is used to solve the Poisson equations to fit the appropriate boundary conditions. We use a similar approach with our hydrodynamic image system. However, due to the more complicated vectorial nature of the fluid flow we need (in addition to a mirror Stokeslet) an additional stresslet and source-dipole contributions [32, 35]:

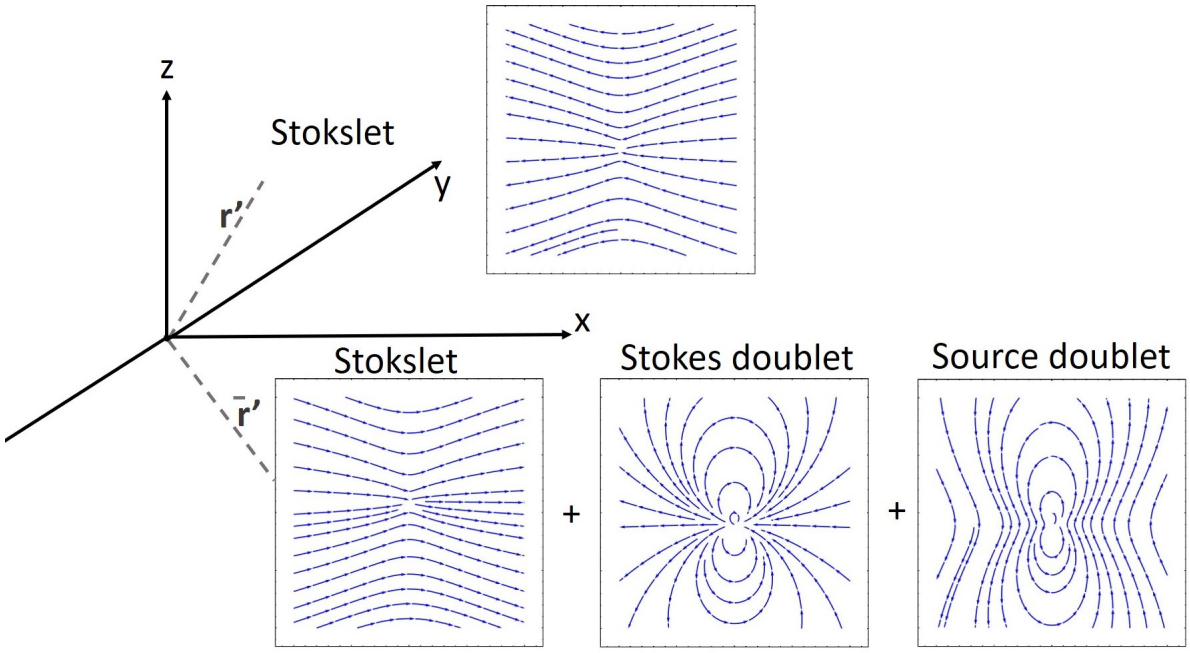

Figure 2: Illustration of a hydrodynamic image system. A Stokeslet is placed at $\mathbf{r}' = (x', y', z')$. An anti-Stokeslet is placed at $\bar{\mathbf{r}}' = (x', y', -z')$. The additional Stokes doublet and Source doublet are also added to satisfy the no-slip boundary condition. Image inspired by reference [35].

The solution that describes a flow field near a boundary and satisfies the no-slip conditions at $z = 0$ is named the Blake tensor. We place our Stokeslet at $\mathbf{r}' = (x', y', z')$ and the image Stokeslet at $\bar{\mathbf{r}}' = (x', y', -z')$. Let us define $\mathbf{r_{rel}} \equiv \mathbf{r} - \mathbf{r}'$ and $\mathbf{R} \equiv \mathbf{r} - \bar{\mathbf{r}}'$. Following the notation of Gauger *et al.* (2009) the Blake tensor yields:

$$\mathbf{G}^B(\mathbf{r}, \mathbf{r}') = \mathbf{G}^O(\mathbf{r} - \mathbf{r}') + \mathbf{G}^{im}(\mathbf{r}, \bar{\mathbf{r}}'), \tag{17}$$

where $\mathbf{G}^O(\mathbf{r} - \mathbf{r}')$ is the Oseen tensor (as described in equation 16) and $\mathbf{G}^{im}(\mathbf{r}, \bar{\mathbf{r}}')$ contains all the mirror contributions. As seen before, the image contributions consist of an image Oseen part $\mathbf{G}^O(\mathbf{r} - \bar{\mathbf{r}}')$ and a part that we call $\delta\mathbf{G}^{im}(\mathbf{r}, \mathbf{r}')$, which contains all the other image contributions (the Stokes doublet and Source doublet). We write $\mathbf{G}^B(\mathbf{r}, \mathbf{r}')$ in the form:

$$\mathbf{G}^B(\mathbf{r}, \mathbf{r}') = \mathbf{G}^O(\mathbf{r} - \mathbf{r}') - \mathbf{G}^O(\mathbf{r} - \bar{\mathbf{r}}') + \delta\mathbf{G}^{im}(\mathbf{r}, \mathbf{r}'), \tag{18}$$

where $\delta\mathbf{G}^{im}(\mathbf{r}, \mathbf{r}')$ can be divided into a source-dipole and stresslet contribution. Hence, we write:

$$\mathbf{G}^B(\mathbf{r}, \mathbf{r}') = \mathbf{G}^O(\mathbf{r} - \mathbf{r}') - \mathbf{G}^O(\mathbf{r} - \bar{\mathbf{r}}') + \mathbf{G}^D(\mathbf{r} - \bar{\mathbf{r}}') + \mathbf{G}^{SD}(\mathbf{r} - \bar{\mathbf{r}}') \tag{19}$$

The Stokes-doublet $\mathbf{G}^D$ and and source-doublet $\mathbf{G}^{SD}$ are defined as [34]:

$$\mathbf{G}^D(\mathbf{r}-\bar{\mathbf{r}}')_{\alpha\beta} = \frac{2z'^2(1-2_{\beta z})}{\mu}\left(\frac{\delta_{\alpha\beta}}{R^3} - \frac{3R_\alpha R_\beta}{R^5}\right) \tag{20}$$

$$\mathbf{G}^{SD}(\mathbf{r}-\bar{\mathbf{r}}')_{\alpha\beta} = \frac{2z'(1-2_{\beta z})}{\mu}\left(\frac{\delta_{\alpha\beta}R_z}{R^3} - \frac{\delta_{\alpha z}R_\beta}{R^3} + \frac{\delta_{\beta z}R_\alpha}{R^3} - \frac{3R_\alpha R_\beta R_z}{R^5}\right) \tag{21}$$

The $\delta\mathbf{G}^{im}(\mathbf{r},\mathbf{r}')$ part of the Blake tensor (containing the stokes and source doublet as visualised in figure 2) can be subdivided in a stresslet and a rotlet contribution (visualized in figure 3 c and d) [34].

The stresslet is a flow profile described by two opposite point forces. Returning to the connection with the image convention in electrostatics, the stresslet can be seen as the second term in the multi-pole expansion which describes the far-away flow field around a force distribution [28]. Below we report the Oseen, image Oseen, stresslet and rotlet contributions to the Blake tensor respectively.

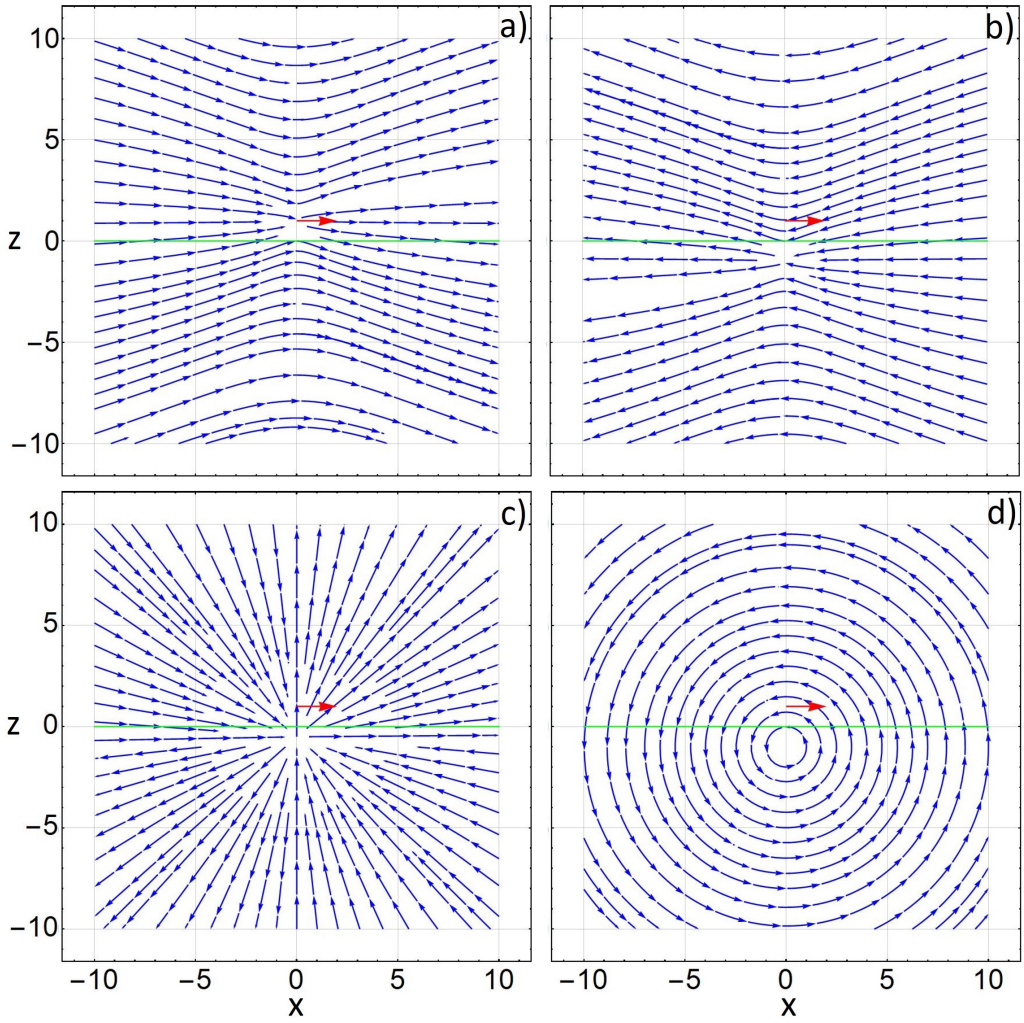

Figure 3: The Oseen and image Oseen, stresslet and rotlet contributions to the Blake tensor are visualized in figure A), B), C) and D) respectively. The fluid flow is represented by the blue streamlines. The red arrow is a representation of the force $\mathbf{f} = (1,0,0)$ that is applied to the fluid.

Supperposing the Oseen, image Oseen, stresslet and rotlet contributions (visualized in figure 3) as described in equation 19 yields in the Blake solution. A visual representation of this is given below:

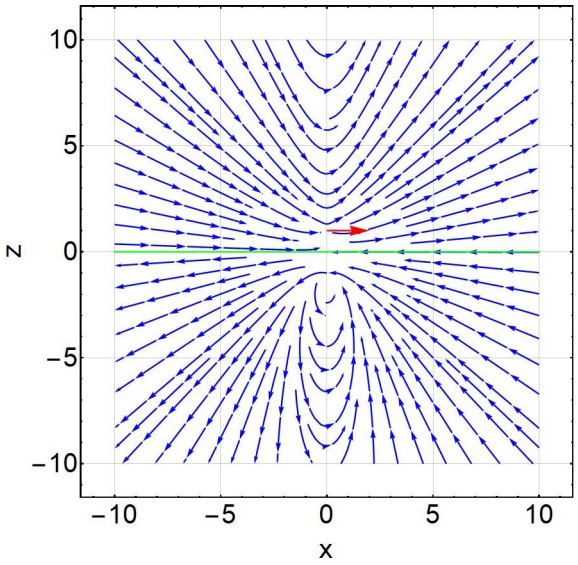

Figure 4: The flow profile of the Blake solution is visualized by the blue streamlines. A point force $\mathbf{f} = (1, 0, 0)$ is applied to the fluid, indicated by the red arrow. The nearby wall is visualized in green.

Pressure field near a cell wall

We wish to describe the traction forces that act on a cell surface. Hence, we need an expression for the pressure inside a fluid. First we will examine the pressure behavior of the bulk system. Analogous to section 3.4 we define $\mathbf{r_{rel}} \equiv \mathbf{r} - \mathbf{r}'$ and $\mathbf{R} \equiv \mathbf{r} - \bar{\mathbf{r}}'$. The pressure $\mathbf{p}(\mathbf{r})$ is linearly related to the point force $\mathbf{r}$ which is applied to the fluid at $\mathbf{r}'$ [31, 35]:

$$\mathbf{p}(\mathbf{r}) = \frac{\mathbf{f}}{4\pi}\mathbf{H}(\mathbf{r} - \mathbf{r}'), \tag{22}$$

here $\mathbf{H}(\mathbf{r} - \mathbf{r}')$ is given by:

$$\mathbf{H}(\mathbf{r} - \mathbf{r}') = \frac{\mathbf{r_{rel}}}{\mathbf{R}^3}. \tag{23}$$

We also wish to examine the pressure behavior in a fluid that is near a boundary that satisfies the no-slip boundary condition. Blake (1971) constructs a Greens function for the pressure. Equivalently to section 3.4 we state the Blake Pressure tensor:

$$\mathbf{H}^B(\mathbf{r}, \mathbf{r}') = \mathbf{H}(\mathbf{r} - \mathbf{r}') + \mathbf{H}^{im}(\mathbf{r}, \bar{\mathbf{r}}'), \tag{24}$$

where $\mathbf{H}^B(\mathbf{r}, \mathbf{r}')$ gives us the total pressure near a wall. Again we have divided the total pressure field into a bulk part $\mathbf{H}$ and a part that contains all the mirror contributions $\mathbf{H}^{im}$. We can subdevide the image contributions in an image bulk part $\mathbf{H}(\mathbf{r} - \bar{\mathbf{r}}')$ and a part that we call $\delta\mathbf{H}^{im}(\mathbf{r}, \bar{\mathbf{r}}')$, which contain all other image contributions. We can write:

$$\mathbf{H}^B(\mathbf{r}, \mathbf{r}') = \mathbf{H}(\mathbf{r} - \mathbf{r}') - \mathbf{H}(\mathbf{r} - \bar{\mathbf{r}}') + \delta\mathbf{H}^{im}(\mathbf{r}, \bar{\mathbf{r}}'), \tag{25}$$

where $\mathbf{H}$ is a defined in equation 23 and reference [35] provides the expression for $\delta\mathbf{H}^{im}$:

$$\delta\mathbf{H}^{im}(\mathbf{r}, \bar{\mathbf{r}}')_{\alpha\beta} = \frac{2z'}{4\pi}\left(\delta_{\alpha i}\delta_{i\beta} - \delta_{\alpha z}\delta_{z\beta}\right)\left(\frac{\delta_{z\beta}}{R^3} - \frac{3R_z^2}{R^5}\right) \tag{26}$$

Using equation 6 and the obtained expression for the pressure near a cell wall allows us to compute the traction forces that work on the cell surface[3].

[3]Note that in equation 26 we use Einstein summation convention

3.5 How spherical particles move in a fluid

When studying low Reynolds number systems we can relate the velocity $\mathbf{v}_i$ of particle i linearly to the external forces $\mathbf{F}$ acting on it. If a point-like particle moves in close proximity to a wall it will induce a flow field described by the Blake solution (see figure 4). However, in this thesis, beating cilia are modeled as spherical particles with a finite size. Consequently, we do not have a point force that acts on the fluid. The fluid moves around the spherical particle and the Blake solution is altered. The flow field created by a moving spherical particle also influences the movement of other particles present in the system. These effects have to be taken into account when studying a system of two cilia. We do so using Faxén's theorem [32] as presented in equation 27. This theorem tells us the velocity of spherical particle i, taking into account the external force acting on the particle (the first term of equation 27), the finite size of the particle and the flow induced by other particles present in the system (the second part of equation 27):

$$\mathbf{v}_i = \frac{1}{6\pi\mu a}\mathbf{F} + \left(1 + \frac{a^2}{6}\nabla^2_{\mathbf{r}_i}\right)\mathbf{u}(\mathbf{r}_i) \tag{27}$$

Here $\mathbf{F}$ is the total force acting on particle i, a is the diameter of the sphere and $\mathbf{u}(\mathbf{r}_i)$ is the flow field induced by other particles present in the system at the position of sphere i. The flow $\mathbf{u}(\mathbf{r})$ induced by another particle at $r' = \mathbf{r_j}$ can be obtained by expanding $\mathbf{G}^B(\mathbf{r}, \mathbf{r'})$. Following reference [32] we obtain the flow field induced by the presence of spherical particle j in the fluid:

$$\boldsymbol{u}(\boldsymbol{r}) \approx \frac{1}{8\pi\mu}\left[\left(1 + \frac{a^2}{6}\boldsymbol{\nabla}^{\mathbf{2}}_{\boldsymbol{r'}}\right)\mathbf{G}^B(\mathbf{r}, \mathbf{r'})\right]_{\boldsymbol{r'}=\boldsymbol{r}_j}\boldsymbol{F}_j, \tag{28}$$

where the second term accounts for the extent through a Faxen derivative. Combining equations 27 and 28 we acquire a relation between the velocity of particle i and hydrodynamic forces acting on it due to the presence of particle j:

$$\mathbf{v}_i = \left[\frac{1}{6\pi\mu a} + \frac{1}{8\pi\mu}\left(1 + \frac{a^2}{6}\nabla^2_{\mathbf{r}_i}\right)\left(1 + \frac{a^2}{6}\boldsymbol{\nabla}^{\mathbf{2}}_{\boldsymbol{r'}}\right)\mathbf{G}^B(\mathbf{r}, \mathbf{r'})\right]\boldsymbol{F}_j \tag{29}$$

In this thesis a system of two neighbouring cilia is studied. Considering only two beads, we write equation 29 in the shorthanded form:

$$\mathbf{v}_i = \sum_{j=1}^{2} G(\mathbf{r}_i, \mathbf{r}_j)\mathbf{F}_j, \tag{30}$$

where G is often referred to as the the total hydrodynamic kernel. It contains information about the radii of the two spheres, their separation and their distance from the wall. It is convenient to split G into two parts. The first part describes the influence of the flow field induced by particle i on itself, called the self-mobility function $\boldsymbol{\mu}_{ii}$. Note that in order to compute this we only have to take into account the image part of the Blake tensor $\mathbf{G}^{im}(\mathbf{r}, \overline{\mathbf{r}}')$. The second part of G contains information about the influence of particle i on particle j, called the a cross-mobility function $\boldsymbol{\mu}_{ij}$. In order to compute this we have to take into account the total Blake Tensor $\mathbf{G}^B(\mathbf{r}, \mathbf{r}')$. The obtained expressions for the self- and cross mobility functions are given below:

$$\boldsymbol{\mu}_{ii}(\boldsymbol{r}_i, \boldsymbol{r}_i) = \frac{1}{8\pi\mu}\left[\frac{4}{3a}\mathbb{I}_3 + \left(1 + \frac{a^2}{6}\boldsymbol{\nabla}^2_{\boldsymbol{r}_i}\right)\left(1 + \frac{a^2}{6}\boldsymbol{\nabla}^2_{\overline{\boldsymbol{r}}_i}\right)\boldsymbol{G}^{im}(\boldsymbol{r}_i, \overline{\boldsymbol{r}}_i)\right] \tag{31}$$

$$\boldsymbol{\mu}_{ij}(\boldsymbol{r}_i, \boldsymbol{r}_j) = \frac{1}{8\pi\mu}\left[\left(1 + \frac{a^2}{6}\boldsymbol{\nabla}^2_{\boldsymbol{r}_i}\right)\left(1 + \frac{a^2}{6}\boldsymbol{\nabla}^2_{\boldsymbol{r}_j}\right)\right]\boldsymbol{G}^B(\boldsymbol{r}_i, \boldsymbol{r}_j) \tag{32}$$

Following reference [14], we define the distance that separates two particles $d = \sqrt{(x_j - x_j)^2 - (y_j - y_i)^2}$. We denote the height of the cilium's beads i and j by z_i and z_j. We assume that the size of the bead a is much smaller than the all the other length scales in our system. Therefore we can ignore all higher order terms of a. The mobility functions reduce to the approximate form:

$$\boldsymbol{\mu}_{ii}(\boldsymbol{r}_i, \boldsymbol{r}_i) \simeq \frac{1}{8\pi\mu}\left[\frac{4}{3a}\mathbb{I}_3 + \boldsymbol{G}^{im}(\boldsymbol{r}_i, \overline{\boldsymbol{r}}_i)\right] \tag{33}$$

$$\boldsymbol{\mu}_{ij}(\boldsymbol{r}_i, \boldsymbol{r}_j) \simeq \frac{1}{8\pi\mu}\boldsymbol{G}^{B}(\boldsymbol{r}_i, \boldsymbol{r}_j) \tag{34}$$

Using the expression for $\boldsymbol{G}^B$ and $\boldsymbol{G}^{im}$ as provided in equations 16, 20, and 21 we can write the components of the self mobility function, for $\boldsymbol{r}_i = \boldsymbol{r}_j$, as:

$$\boldsymbol{\mu}_{ii}(\boldsymbol{r}_i, \boldsymbol{r}_i) \simeq \frac{1}{6\pi\eta a}\begin{pmatrix} 1-\epsilon & 0 & 0 \\ 0 & 1-\epsilon & 0 \\ 0 & 0 & 1-2\epsilon \end{pmatrix}, \tag{35}$$

where $\epsilon = (9a/16z)$. For $\boldsymbol{r}_i \neq \boldsymbol{r}_j$ we additionally assume that the height of both beads above the surface is much small than the distanced that separates them: $z_i, z_j \ll d$. We expand equation 34 to the first order. Doing this we can approximate the components of the cross mobility function as:

$$\boldsymbol{\mu}_{ij}(\boldsymbol{r}_i, \boldsymbol{r}_j) \simeq \frac{3}{2\pi\eta}\frac{z_i z_j}{d^3}\begin{pmatrix} \cos^2\psi & \sin\psi\cos\psi & 0 \\ \sin\psi\cos\psi & \sin^2\psi & 0 \\ 0 & 0 & 0 \end{pmatrix}, \tag{36}$$

where ψ is defined as $\tan\psi = (y_j - y_i)/(x_j - x_i)$.

Let us consider the mobility functions corresponding to a system of two cilia. Using the obtained mobility functions the total hydrodynamic kernel G now reads:

$$G_{1,2} = \begin{pmatrix} \boldsymbol{\mu}_{11}(\mathbf{r}_1, \mathbf{r}_1) & \boldsymbol{\mu}_{12}(\mathbf{r}_1, \mathbf{r}_2) \\ \boldsymbol{\mu}_{21}(\mathbf{r}_2, \mathbf{r}_1) & \boldsymbol{\mu}_{22}(\mathbf{r}_2, \mathbf{r}_2) \end{pmatrix} \tag{37}$$

We substitute the total hydrodynamic kernel G back in equation 30 and rewrite this in the form:

$$\begin{aligned} \mathbf{f}_1 &= M_{11}\mathbf{v}_1 + M_{12}\mathbf{v}_2 \\ \mathbf{f}_2 &= M_{12}\mathbf{v}_1 + M_{22}\mathbf{v}_2 \end{aligned} \tag{38}$$

Here the matrices M_{ij} are the components of the total mobility matrix M, which denotes the inverse the G. When we consider a single cilium we can ignore the cross mobility terms. Therefore equation 38 reduces to:

$$\mathbf{f}_1 = M_{11}\mathbf{v}_1 \tag{39}$$

Finally, we explore the influence of a spherical particle on the surrounding substrate. When we consider a system of a single cilium the force applied to the fluid is given by equation 39. The force is linearly related to the fluid velocity $\mathbf{u}(\mathbf{r})$ as explained in section 3.4. When considering a spherical particle near a wall we have to take into account the total Blake tensor. The fluid velocity yields:

$$\mathbf{u}(\mathbf{r}, t) = \mathbf{G}^B(\mathbf{r}, t)M_{11}(\mathbf{r}, t)\mathbf{v}(\mathbf{r}, t) \tag{40}$$

4 Description of the model

In order to model a beating cilium and study the hydrodynamics effects on the surrounding substrate we have to dispense a minimal model that captures the essential features of a ciliated system. A minimal model is provided by Vilfan and Jülicher (2006). In this model a cilium is replaced by a small moving sphere with radius a (see figure 5). This model can be used to study the hydrodynamic far field generated by a beating cilium using only a few parameters that characterize the geometry of the beating pattern [1]. By specifying these parameters the model captures the essential features like the difference between the effective and recovery stroke. In this case there is no need for a detailed description of the actual shape of the cilium [33]. However, the model cannot be used to study the hydrodynamic flow field near a beating cilium as that depends on the detailed motion the cilium exhibits [1]. A visualization of the minimal model is presented below. The data for the full beating pattern of the cilium is provided by Perugachi Israels [2]:

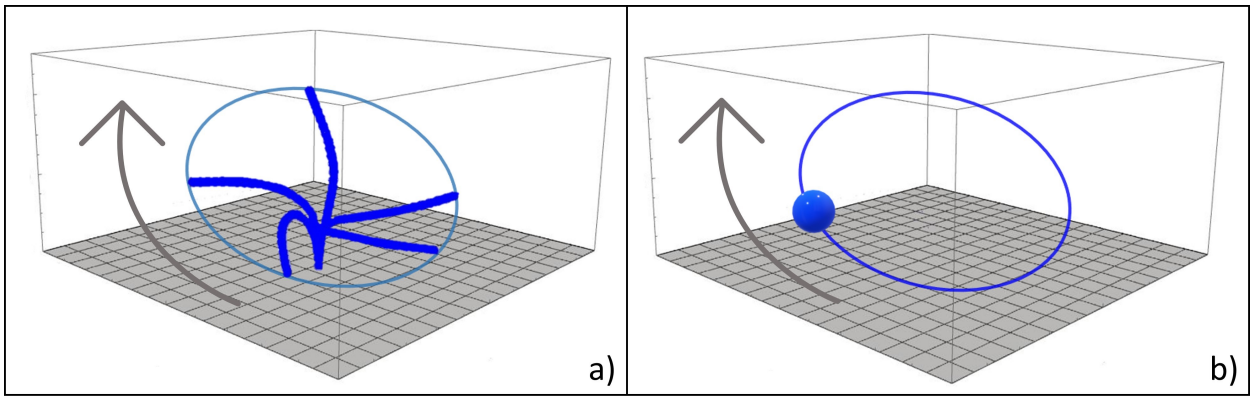

Figure 5: Figure a: a schematic beating pattern of a cilium with a different effective and recovery stroke. Figure b: a cilium is replaced by a small moving sphere with radius a. The bead moves on a fixed tilted elliptic trajectory near a surface placed at $z = 0$. The tilt in the trajectory reflects the asymmetry of the beating pattern.

Note that only a tilted trajectory can generate a net flow. We can argue this intuitively by dividing the trajectory into two parts; a part where the bead is located far away from the wall and a part where the bead is near the wall. The movement of the bead is generated by a constant internal force. In the part of the trajectory where the bead is closest to the wall, it experiences more friction making it move slower. The friction far away from the wall is much smaller. As a result the cilium moves faster in this part of the trajectory. In a low-Re system this results in a larger fluid velocity. Consequently, the motion of a cilium in the far away part of the trajectory determines the direction of the flow. In a typical trajectory of a cilium, as shown in figure 5, the direction of the flow points from left to right. The perpendicular parts of the trajectory (where the bead mainly moves up and down) contribute to the flow perpendicular to the wall. When considering a system of many cilia, the flow perpendicular to the wall averages to zero [14].

We denote the position of the bead by $\mathbf{r}^b[\phi(t)]$ which depends on the phase of the oscillation, described by an angle ϕ. The elliptical trajectory, with major axis A and minor axis B is tilted around the x, y and z axis with angles α, β and γ respectively. This rotation is denoted by rotation matrices $\mathcal{R}_x(\alpha)$, $\mathcal{R}_y(\beta)$ and $\mathcal{R}_z(\gamma)$. A parametric representation of the position of the bead follows:

$$\mathbf{r}^b[\phi(t)] = \begin{bmatrix} x \\ y \\ z \end{bmatrix} + \mathcal{R}_x(\alpha)\mathcal{R}_y(\beta)\mathcal{R}_z(\gamma) \begin{bmatrix} A\cos\phi \\ B\sin\phi \\ 0 \end{bmatrix} \tag{41}$$

Here x, y and z describe the position of the centre of the cilium's elliptical orbit.

4.1 The minimal model and the advanced model

By defining the parameters we impose the position of the bead at all times t. To determine these parameters we compare the trajectory of the bead (representing the tip of the cilium) to the beating pattern of a fully modeled cilium. Such a model is provided in a in a study done by Perugachi Israels [2]. In this study the three individual strands of the cilium are modeled. Each strand consists of 24 beads with diameter $a = 1$, connected to each other by springs. The strands are arranged in a triangular structure and are also connected to each other by springs. The model is based on the beat pattern of nodal cilia in mice as described in reference [7] and section 2.

In the advanced model by Perugachi Israels the tip of the cilium describes a elliptic-like orbit (see figure 6). Data provided by Perugachi Israels supplies us with the position of the tip of the cilium during 30 snapshots, which cover exactly one orbit. During this section we will report the reduced time t^* of one snapshot. We denote the position of the tip of the cilium in the advanced model by $\mathbf{r}^t(t^*)$. Following the model by Vilfan and Jülicher (2006) [1], we assume that our beat represents the tip of this cilium. We fit the trajectory of our bead $\mathbf{r}^b$ (on a fixed elliptic orbit) to the tip of the cilium $\mathbf{r}^t$ (on a elliptic-like orbit):

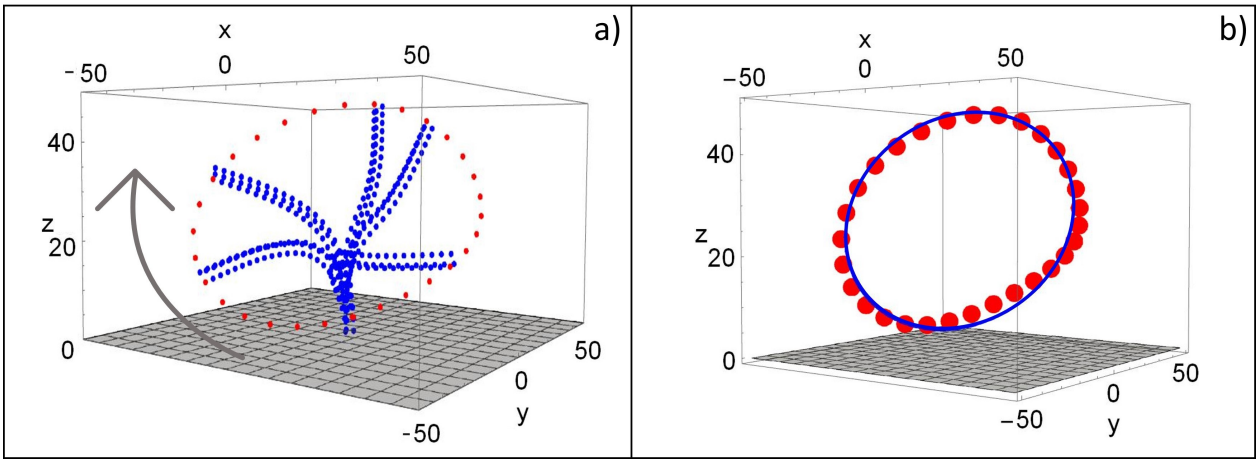

Figure 6: Figure a: the trajectory of the cilium in the model by Perugachi Israels [2]. The red dots denote the elliptic-like orbit the tip of the cilium creates, data for the figures provided by Perugachi Israels [2]. Figure b: the best elliptic fit to this model. The red spheres represent the cilium-tip trajectory of penal (a). The blue line is the best elliptic fit. The cilium rotates clockwise (the direction of the gray arrow).

In this section we will elaborate upon how this fit is established. We first determine the (mean) centre and major/minor axes of the elliptic-like orbit described by the tip of the cilium in the advanced model denoted by $\mathbf{r}^t$. We use these parameters for the elliptic trajectory of the bead denoted by $\mathbf{r}^b$. We continue by minimizing the difference that is left between $\mathbf{r}^t$ and $\mathbf{r}^b$. By doing so we obtain the tilt of the ellipse.

In order to determine the position of the (mean) centre of the orbit of the cilium-tip we extract the maximum and minimum values of the components of $\mathbf{r}^t$ and find: $\mathbf{r}^t_{\max} = (39.27, 20.58, 49.19)$ and $\mathbf{r}^t_{\min} = (-33.88, -42.13, 8.57)$. Averaging this we obtain the the mean centre of the elliptic like orbit: $\mathbf{r}^c = (2.70, -10.78, 28.87)$. This position is used as the centre of the fixed elliptic orbit $\mathbf{r}^b$ *viz.* the (x, y, z) components of equation 43. A visualization of this procedure is given in figure 7a.

In order to determine the major and minor axes of the elliptic-like orbit $\mathbf{r}^t$ we define $\mathbf{d}(t^*) = \mathbf{r}^t(t^*) - \mathbf{r}^c$, the distance from the tip of the cilium to the (mean) center $\mathbf{r}^c$ during one period. From this we extract the maximum and minimum distance: $|\mathbf{d}(t^*)|_{\max} = 37.96$ and $|\mathbf{d}(t^*)|_{\min} = 35.27$ and use these as the major and minor axes A and B of the (fixed) elliptic orbit $\mathbf{r}^b$. A visualization of this procedure is given in figure 7b.

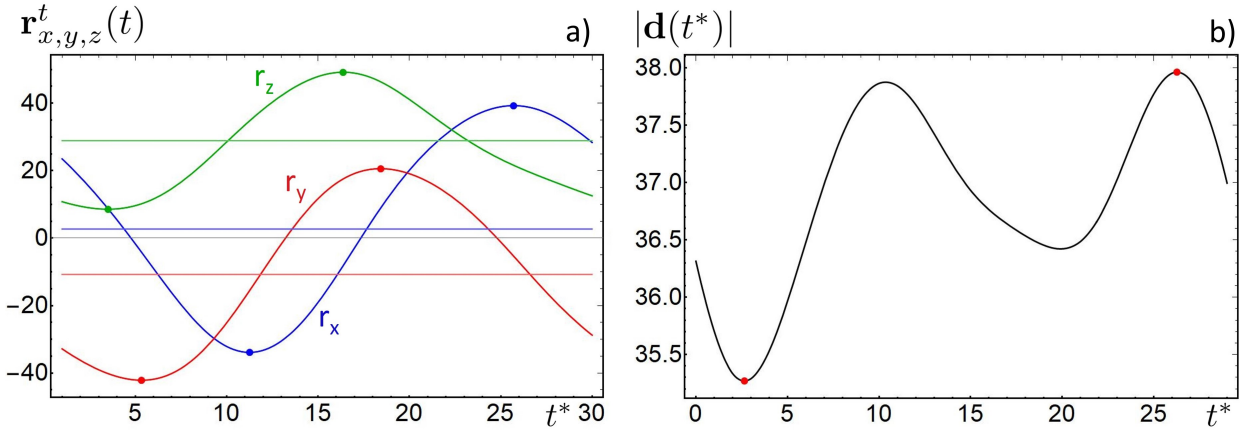

Figure 7: Data for both figures provided by Perugachi Israels [2]. Figure a: the x, y and z components of $\mathbf{r}(t^*)$, denoting the position of the tip of the cilium as a function of the reduced time (30 snapshots during one period). The maximum and minimum coordinates are determined as indicated by the colored dots. The mean values of the x, y and z components of $\mathbf{r}(t)$ are plotted (the horizontal lines). The mean centre of the ellipse follows: $\mathbf{r}^c = (2.70, -10.78, 28.87)$. Figure b: the distance from the tip of the cilium to the (mean) center $\mathbf{r}^c$ during one period. Here $|\mathbf{d}(t^*)| = |\mathbf{r}(t^*) - \mathbf{r}^c|$. The maximum and minimum distance are 37.96 and 35.27 respectively, denoted by the red dots.

We continue determining the tilt of the ellipse. In order to do this the remaining difference between $\mathbf{r}^t$ and $\mathbf{r}^b[\alpha, \beta, \gamma, \phi(t)]$ has to be minimized with respect to α, β and γ. Using the previously obtained centre and major and minor axes, we define a function that describes the remaining difference:

$$\Delta\mathbf{r}[\alpha, \beta, \gamma, \phi(t)] = \sum_{i=1}^{3} \max\{|\mathrm{r}^b_i - \mathrm{r}^t_{\max\, i}|\} + \sum_{i=1}^{3} \min\{|\mathrm{r}^b_i - \mathrm{r}^t_{\min\, i}|\} \tag{42}$$

We minimize equation 42 and obtain: $\alpha = 0.175\pi$, $\beta = 0.075\pi$ and $\gamma = 0.05\pi$. The obtained values describe the angle that minimize the remaining difference between the elliptic trajectory of the minimal model and the elliptic-like trajectory of the advance model by Perugachi Israels.

The trajectory of the bead in the minimal model is now completely obtained nad yields:

$$\mathbf{r}^b[\phi(t)] = \begin{bmatrix} 2.70 \\ -10.78 \\ 28.87 \end{bmatrix} + \mathcal{R}_x(0.175\pi)\mathcal{R}_y(0.075\pi)\mathcal{R}_z(0.05\pi) \begin{bmatrix} 37.96\cos\phi \\ 35.27\sin\phi \\ 0 \end{bmatrix} \tag{43}$$

Using the fully obtained trajectory of the bead, we define the normal to the trajectory at each time step. The averaged normal over one period makes an angle of 35° with respect to the z axes. This is well within the range of experimentally observed cilium tilt, as described in in section 2.

Below, we present a projection of the elliptic orbit on the x,y plane. Viewed from above the bead is moving clockwise on the fixed trajectory. The height of the bead is represented by the color map.

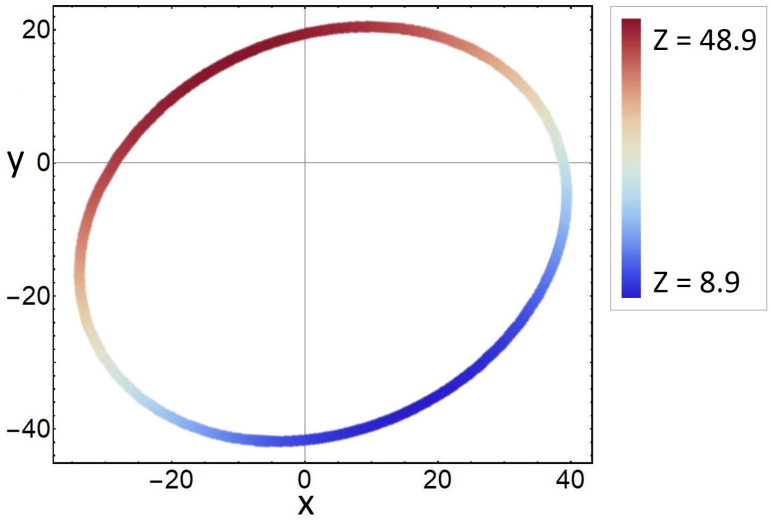

Figure 8: A projection of the elliptic orbit on the x, y plane. The height of the orbit is visualized; red corresponds to the highest point and blue to the lowest point of the bead in the orbit.

Analyzing this orbit we can intuitively argue that the expected direction of the net fluid flow points from left to right. This is based on the same argumentation as in section 4, where is explained that the effective part of the cilium stoke determines the net flow direction. At the highest point in the orbit the bead (which represent the cilium tip) is located around $z \sim 50$. In this part of the effective stroke the cilium is in its most extended form. Using the length of the cilium we relate 50 model units to 5 μm i.e. 1 model unit of length corresponds to 0.1μm. This is a rough estimation, as we have no actual cilium shape or associated length in the minimal model. The converted numerical values can therefore only be used to gain insight into the order of magnitude.

4.2 Force balance in ciliated systems

To complete the equations of motion we need to supply an expression for the internal forces that generate ciliary motion. Again, the description of the force should capture the essential features of a ciliated system. In particular, we have to take into account that the local drag forces are greater near the wall, and are related to the local velocity.

Gray and Hancock [36] were the first to propose a method to describe the relation between the local drag force and local velocity. They divide the drag forces into a tangential, normal and binormal components. They assume the components are proportional to the respective components of the velocity, with different proportionality constants. This model is simple to implement and therefore used in many simulations [33, 36].

We assume the active mechanism in the cilium generates a tangential force $\boldsymbol{f}_i = f_i \hat{\boldsymbol{t}}_i$. Following Gray and Hancock we can relate the tangential force to the tangential components of the velocity $\boldsymbol{v}_i = v_i \hat{\boldsymbol{t}}_i$. Here $\hat{\boldsymbol{t}}$ is a unit vector tangent to the trajectory of the cilium $\boldsymbol{t_i} = d\boldsymbol{r}_i/d\phi_i$. Because we study laminar flows, we relate the two in a linear fashion: $f_i = f_0 - \kappa v_i$, with proportionality constant $\kappa = f_0/6\pi\eta a v_0$. Here f_0 denotes the force necessary to stop the motion of the cilium and v_0 denotes the velocity of a cilium when no external force is applied [14].

The total force $\boldsymbol{F}_i$ acting on the beat is generally not parallel to the direction of the motion. There are not only tangent forces but also normal forces. Otherwise the sphere would not be moving on a closed ellipsoidal track. The total force $\boldsymbol{F}_i$ therefore yields:

$$\hat{\boldsymbol{t}} \cdot \boldsymbol{F}_i = f_0 - \kappa v_i \tag{44}$$

For a cilium we have the typical values: $f_0 \sim 10\,\mathrm{pN}$, $a \sim 10\mu\,\mathrm{m}$, $v_0 \sim 100\mu\, ms^{-1}$ [14, 37]. We use this to estimate $\kappa \sim 1$. Using this we can write equation 45 as follows:

$$\hat{\boldsymbol{t}} \cdot \boldsymbol{F}_i = f_0(1 - v_0^{-1} v_i) \tag{45}$$

We can write the velocity as $\boldsymbol{v}_i = \dot{\phi}_i \hat{\boldsymbol{t}}_i$. When only considering the tangential component an expression for internal force that generates ciliary motion follows:

$$\hat{\boldsymbol{t}} \cdot \boldsymbol{F}_i = f_0(1 - v_0^{-1} |\mathbf{t}_i| \dot{\phi}_i) \tag{46}$$

The force is balanced by the hydrodynamic friction as described in equations 38. When combing the two we obtain a system of coupled differential equations:

$$\begin{aligned} \dot{\phi}_1 \left(\mathbf{t}_1^T M_{11} + (f_0/v_0)|\mathbf{t}_1|\right) + \dot{\phi}_2 \mathbf{t}_1^T M_{12} \mathbf{t_2} &= f_0 \\ \dot{\phi}_1 \mathbf{t}_2^T M_{21} \mathbf{t_1} + \dot{\phi}_2 \left(\mathbf{t}_1^T M_{22} + (f_0/v_0)|\mathbf{t}_2|\right) &= f_0 \end{aligned} \tag{47}$$

Solving equation 47 reveals the dynamics of the phases of two cilia. When considering a single cilium we do not have to take into account the interaction terms, meaning we set $M_{i,j}$ for $i \neq j$ to zero.

To solve this system of coupled differential equations we have to describe values to f_0, v_0 and a. These parameters determine the state of motion for a cilium. Once more we compare the trajectory of our bead $\mathbf{r}^b$ to the tip of the cilium $\mathbf{r}^t$. In this comparison we use the previously obtained tilt and values for the major/minor axes. In figure 9 we visualize the components of the position vectors of both models during one orbit. When we increase a the bead will experience more friction. Therefore, it will move slower in the part of the trajectory near the wall. When we increase the force f_0 the bead will move faster through the orbit. By fitting the accurate ratio of the two we impose that the period of one bead cycle in the two models is equal. Additionally, we impose that the two beads are at the highest and lowest points in the orbit at approximately the same time.

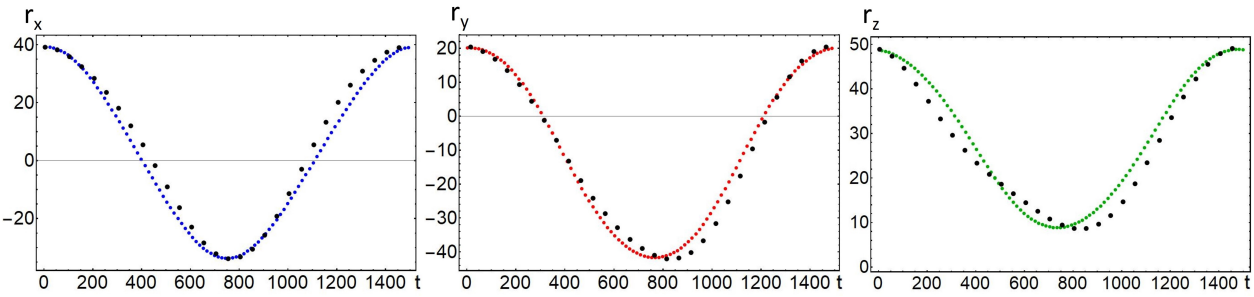

Figure 9: The colored data represents the the x, y and z components of the position of bead during on orbit, in blue, red and green respectively. The black dots present the x, y and z components of the position of the bead on the elliptic-like orbit during one period, this data is provided by Perugachi Israels [2].

For a viscosity of $\eta = 1$ we obtain $a = 1$, $f_0 = 112.3$ and $v_0 = 5.96$. The modeled bead completes one orbit in 1500 time steps, corresponding to an experimentally observed frequency of 10 Hz. Using this we relate 1 time step in the model to 6.6×10^{-5}s. Using the obtained size of the bead we compute the height-with ratio and observe that it is in the same order of magnitude as experimentally observed values.

5 Results - Studying a single ciliated system

In this section we will present the results obtained from analyzing a minimal model of a single cilium. We will first present the dynamics of our ciliated system i.e. the position of the bead, the velocity along the trajectory and the phase variable $\phi(t)$. We continue by examining the the influence of the moving bead on the surrounding substrate. In order to do this we present the fluid velocity and the traction on the cell surface. The results of of the minimal model are presented in blue during the entire section. We compare these results to the results obtained by Perugachi Israels, which are presented in red.

5.1 Fluid velocity in a ciliated system

We examine a single ciliated system. The centre of the elliptic orbit is placed at $\mathbf{r}^c = (2.70, -10.78, 28.87)$. For further specification of the system see section 4. By solving differential equation 47 we obtain phase variable $\phi_1(t)$. The phase speed is denoted as $\dot{\phi}_1(t)$, the time derivative of $\phi_1(t)$. Using the phase variable and equation 43 the position of the bead $\mathbf{r}_1(t)$ is obtained. We denote the velocity of the bead along the trajectory as $\dot{\mathbf{r}}(t) = \mathbf{v}_1(t)$. The dynamics of a single ciliated system are presented below:

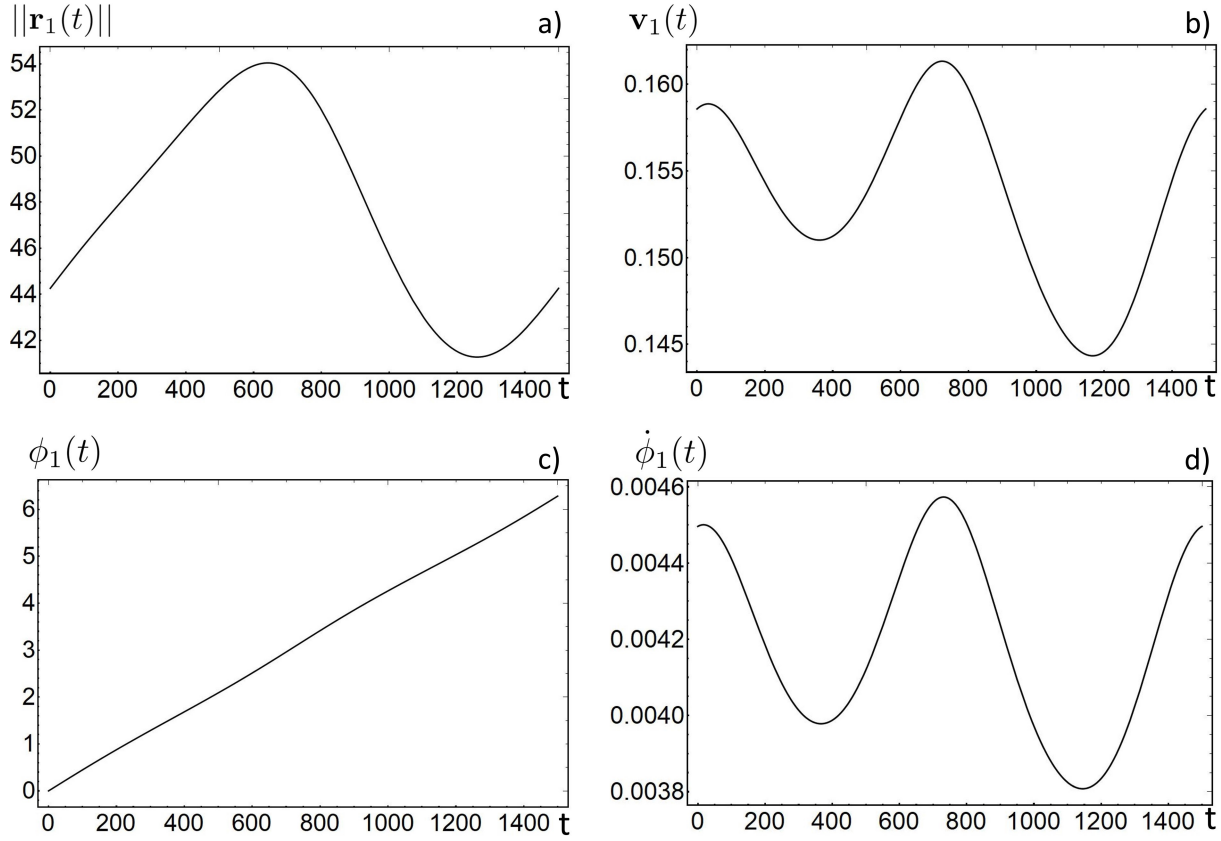

Figure 10: Figure a: the norm of the position of the bead during one orbit. Figure b: the velocity of the bead during one orbit. Figure c: the phase variable ϕ during one orbit. Figure d: the phase speed during one orbit. Here $\dot{\phi}(t)$ denotes the time derivative of the $\phi(t)$.

We continue by investigating the effect of the bead on the surrounding substrate. Using equation 40 we obtain the fluid velocity $\mathbf{u}(\mathbf{r})$. In order to normalize this we divide through the maximum speed of the bead. In figure 11 we examine snapshots of the fluid velocity at two times t, half a period apart.

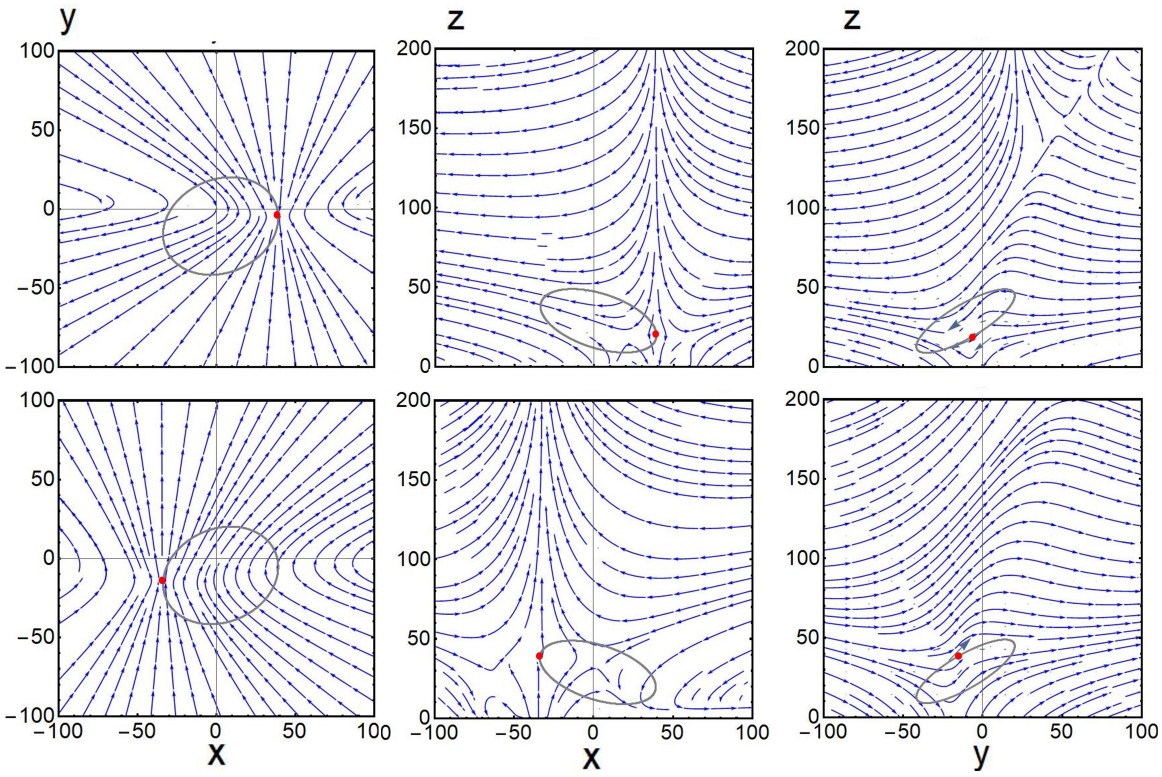

Figure 11: The blue arrows visualize the flow field generated by a moving bead on a elliptic orbit. A snap shot in time is taken at $t = 0$ (upper figures) and half a period later (figures on the bottom), the position of the bead at the corresponding time is denoted by the red dot. The cross sections are taken in the plane of the position of the bead.

Next, we examine the fluid velocity $\mathbf{u}(\mathbf{r}, t)$ during one period, at a fixed point in the fluid. We consider two points in the plane of the centre of the ellipse and one point above the centre of the ellipse, all points are about two cilium lengths away from the center point. Again we report the normalized fluid velocity.

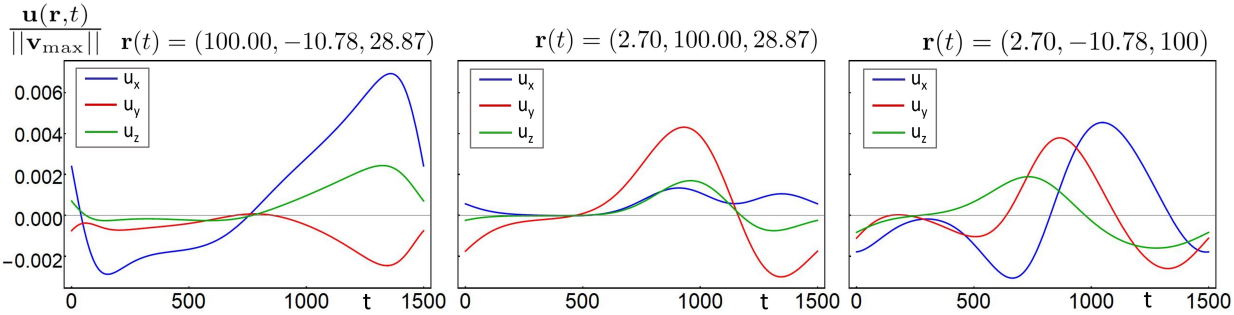

Figure 12: The (normalized) fluid velocity $\mathbf{u}(t)$ at three different points in the fluid are visualized during one orbit. The x, y and z components of $\mathbf{u}(t)$ are shown in blue, red and green respectively.

The asymmetry in the graphs of figure 12 indicate the presence of a net fluid flow. We define the net fluid flow $\mathbf{u}_{\text{mean}} = \frac{1}{T}\int_0^T \mathbf{u}(\mathbf{r}, t)dt$. Here, T is the time in which the bead completes one orbit. Using this, a mean fluid velocity of 0.0069 (in model units) is observed at $\mathbf{r}(t) = (100.00, -10.78, 28.87)$ (the left image of figure 12). At this point the maximum fluid velocity is 0.0014. This results in a maximum deviation

of the mean fluid velocity of 0.0058. In all components of the fluid velocity the mean value is of the same order as magnitude as the maximum deviation form the mean. This justifies the comparison between the net fluid flow generated by the minimal model to the advanced model in figure 13. Here, we compute the net fluid velocity at various regions in the fluid: along lines parallel to the x, y and z axes (the upper, middle and bottom parts of figure 13). The lines go through the centre point of the ellipse. The x, y and z components of the fluid velocity are presented separately (the left, middle and right parts of figure 13). The results obtained from the minimal model are visualized in blue. We compare these quantities to the advanced model by Perugachi Israels, whose data is presented in red. We report the normalized net fluid velocities below:

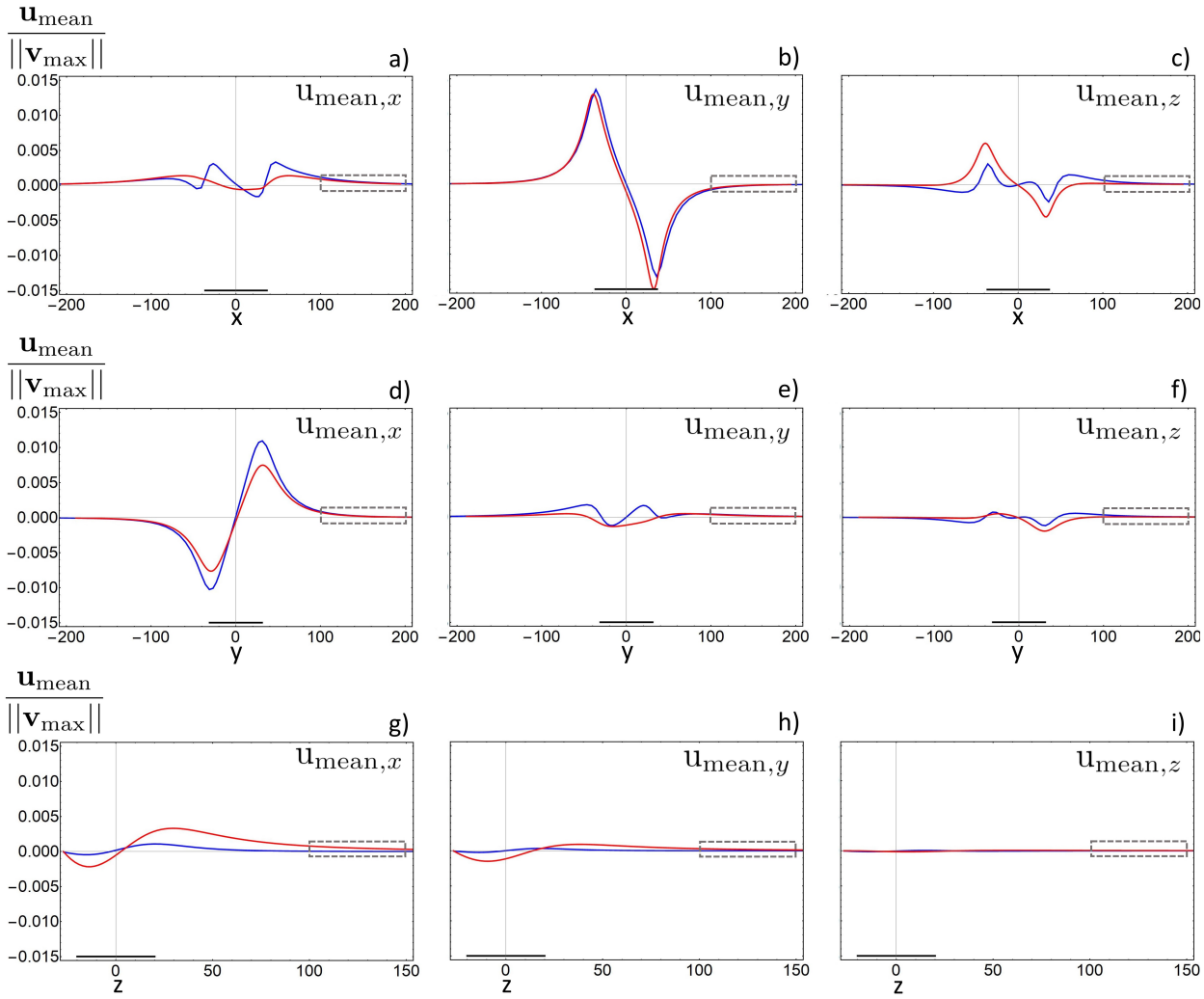

Figure 13: In the upper row we visualize the averaged normalized fluid velocity $\mathbf{u}_{\text{mean}}$ along a line parallel to the x axis, going through the centre point of the ellipse. The y and z position in the fluid are fixed at the centre point of the ellipse. The x, y and z components of $\mathbf{u}_{\text{mean}}$ are presented in the left middle and right figures respectively. The blue data corresponds to the net fluid flow generated by the model of a spherical bead on a fixed elliptic orbit. The red data is provided by Perugachi Israels. The fluid velocity along lines parallel to the y and z axes are visualized similarly in the middle and bottom row of this figure. The black bar is a representation of the ellipse along the corresponding axes. The dashed boxes are visualized in more detail in figure 14. Note that the centre of both ellipses are re-centred around zero.

In penal a-f of figure 13 the fluid velocities generated by the minimal model and the more advanced model are visualized at $\sim 3\,\mu$m (in converted units, see section 4) above the cell surface (this is in the plane of the centre of the elliptic orbit). When comparing the minimal model to the advanced model we notice similarly placed and shaped peak values in the fluid velocity components perpendicular to the motion of the bead, as can be seen in figure 13b,d. For the peak values we observe a difference in fluid velocity between the two models of $\sim 14\%$ and $\sim 37\%$, respectively. In addition to this we observe that the behavior of the decay in both models is similar. For the other components of the fluid velocity (at $\sim 3\,\mu$m above the cell surface) the difference between the two models is slightly more pronounced; the peak values are shaped en positioned differently. Here, the maximum observed difference between the models is roughly 50%. In figure 13 g-h we present the difference between the minimal model and advanced model along a line normal to the surface, going through the elliptic orbit's center. In the region close to the centre point of the ellipse the peak values in the two models generally differ $\sim 70\%$. The decay of the fluid velocity as a function of the distance also appears to behave very differently in both models.

When examining the fluid velocity close to the ellipse, we surprisingly observe that the minimal model captures many of the properties of the more advanced model. In the direction where most of the fluid movement is generated (perpendicular to the direction of the motion of the bead) the two models correspond best. However, the difference between the two models is more pronounced when examining the fluid above the ellipse. To further investigate examine the fluid velocity profile of both models further away (>2 cilium lengths away) from the centre point of the elliptic orbit. In order to to this the dashed boxes in figure 13 are magnified in the figure below:

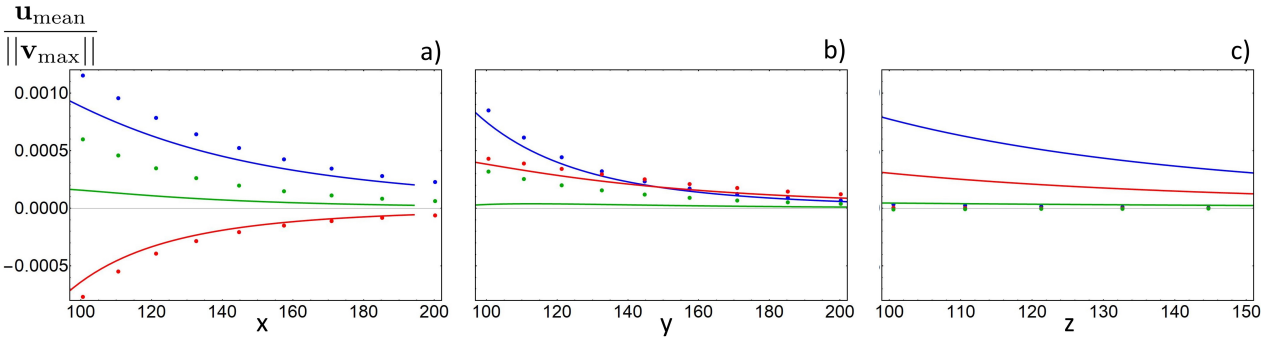

Figure 14: The doted data presents the fluid velocity generated by the minimal model. We examine regions along lines parallel to the x, y and z axes, going through the centre of the elliptic orbit (left, middle and right figure). The x, y and z components of the averaged fluid velocity are visualized separate in blue, red and green, respectively. The lines are a representation of the fluid velocity generated by the advanced model. This data is provided by Perugachi Israels [2].

Studying the above figure we immediately note that the x and y components of the fluid velocity in both models look very similar. Here, at 2 cilium lengths away from the center point at $\sim 3\,\mu$m above the surface, we observe a difference in the x and y component of the fluid velocity of $\sim 30\%$ and $\sim 10\%$, respectively. However, when examining the z component of the fluid velocity the observed differences are $\sim 75\%$ and $\sim 95\%$, respectively. The observed differences between the two models stay roughly the same when examining the fluid further away (~ 4 cilium lengths). We compare the decay of the fluid velocity between the two models and observe a similar (power-law) trend in each compared component. In figure 14c we present the fluid velocities generated by both models above the cilium. We immediately notice the sizable difference between the two models, the decay in fluid velocities do not follow the same trend. In addition to this, the minimal model generates far less fluid motion compared to the advanced model. The maximum difference is observed in the x component of the fluid velocity, *viz.* 97%.

The inability to generate fluid motion in the region above the cilium is one of the weaknesses of the minimal model. The origin thereof can be traced to approximation made in the minimal model, consisting of only one bead. Therefore, the extending and bending of the cilium during the effective and recovery stroke is not fully captured. In the advanced model the additional beads all move up and down during the bending and stretching of the cilium. Consequently, more fluid motion is generated in the direction perpendicular to the cell wall. However, the fluid velocity in this direction is much smaller than the fluid flow parallel to the nearby boundary at $\sim 3\,\mu$m above the cell surface.

Finally, the normalized fluid velocity generated by the minimal model is presented below.

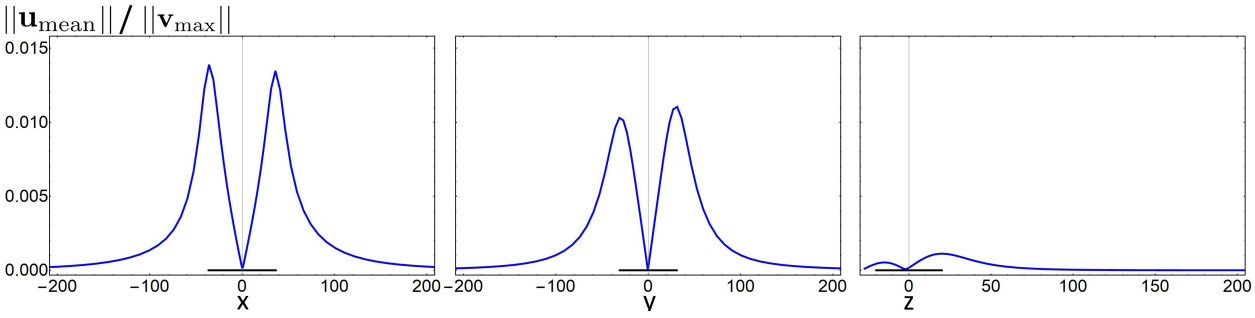

Figure 15: The norm of the fluid velocity generated by the minimal model. We present this along lines parallel to the x y and z axes, going through the centre of the elliptic orbit.

Studying figure 15 we immediately note that the peaks in fluid velocity occur around the edge of the elliptic trajectory. Comparing the peak values in each figure we observe that the highest peaks are located in the negative x and positive y direction. The peaks are both $\sim 7\%$ bigger than the other peak value in the graph. This observation strongly hints towards a general flow direction from left to right. This is in agreement with the experimentally observed direction in the flow (see section 2) and with the theoretically expected flow direction (see section 4). We compute the fluid velocity generated by the minimal model at $\sim 3\,\mu$m above the surface at two cilium lengths away from the cilium. We observe a converted fluid velocity of $\sim 1.5\,\mu\text{ms}^{-1}$, which is in the same order of magnitude as experimentally observed values.

5.2 Stress on surface induced by a single cilium

We examine the traction forces $\mathbf{T}(\mathbf{r}, t)$ that act on the cell surface using equation 7 and the expression for pressure field near a cell wall as provided in section 3.4. We examine the traction at two times t and present snapshots taken at $t = 0$ and at a quarter period later:

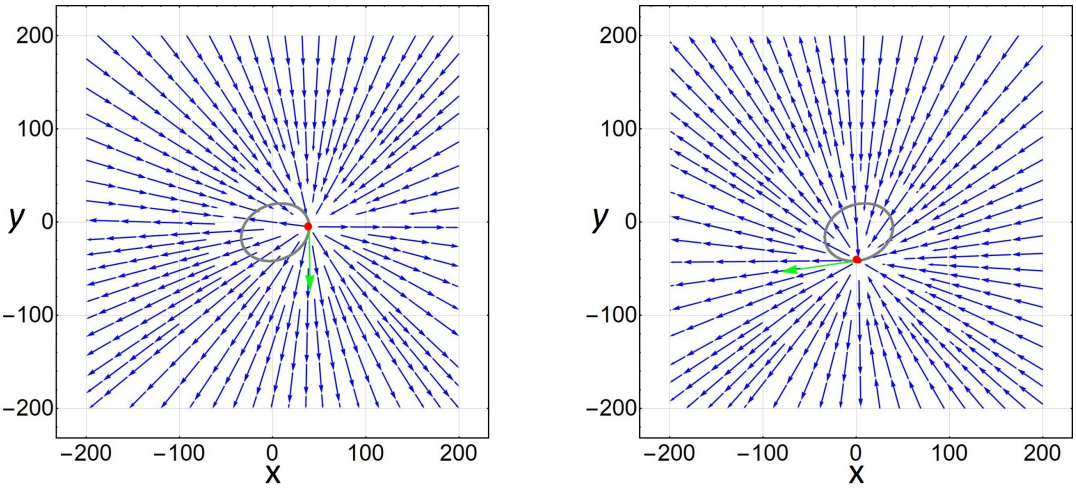

Figure 16: A visualization of the traction (blue arrows) acting on the cell surface. A snapshot at $t = 0$ is presented in the left figure, a snap shot a quarter period later is presented in the right figure. The position of the bead at the corresponding time is denoted by the red dot. The green arrow represents the force.

Next, we examine the traction forces during one period at a fixed point in the fluid. We consider two point at the surface at ~ 2 cilium lengths away from the centre point of the elliptic orbit.

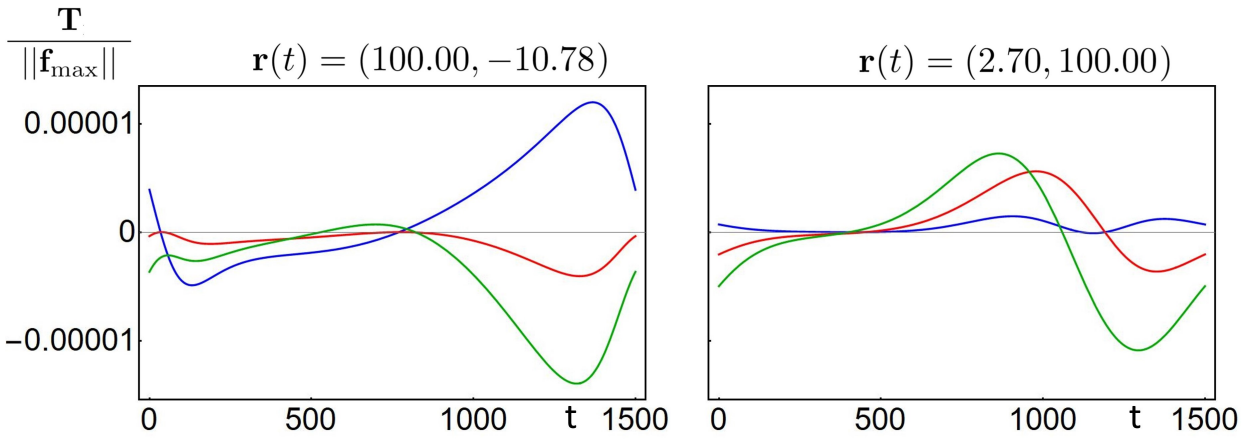

Figure 17: A visualization of the traction forces that act on the surface generated by the minimal model. The x, y and z components are presented in blue, red and green, respectively. Two fixed point on the left and right of the elliptic trajectory are presented in this figure.

Analogous to section 5.1 we define the net traction over one period $\mathbf{T}_{\text{mean}} = \frac{1}{T}\int_0^T \mathbf{T}(\mathbf{r},t)dt$. We report this at $\mathbf{r}(t) = (100.00, -10.78)$ (left image of figure 17) and we observe that the x component of the net traction here yields: 1.20×10^{-5}. At this point the maximum traction generated by the minimal model is observed: 2.21×10^{-5}. This results in a maximum deviation of the average of 1.01×10^{-5}. In all components of the generated traction the mean value is of the same order of magnitude as the maximum deviation from the mean. Following the same argumentation as before we now compare the net traction generated by the minimal model to the model by Perugachi Israels. Her data is presented in red.

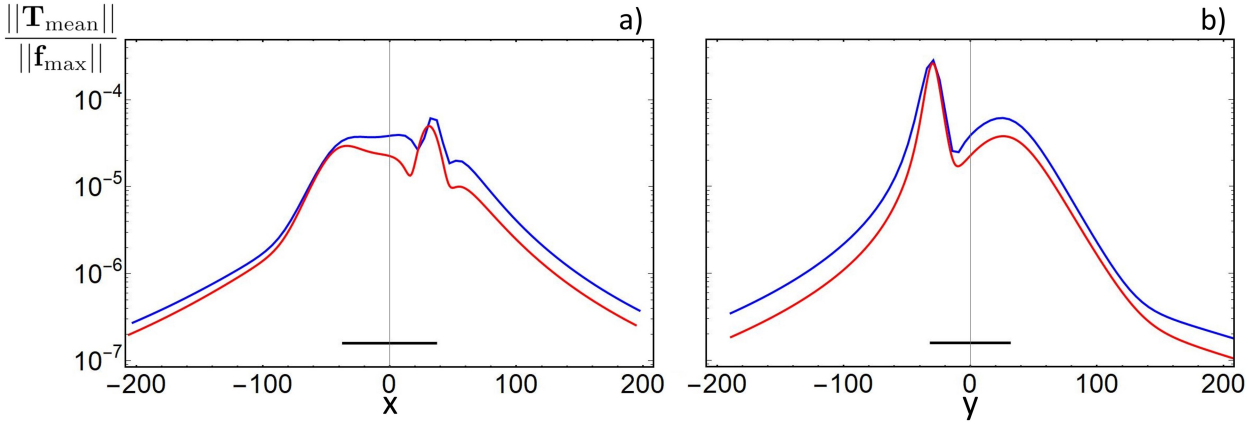

Figure 18: The normalized traction averaged over one period is visualized. The blue data presents the traction generated by the minimal model. The red data is provided by Perugachi Israels. Figure a: we present the traction along a line parallel to the x axis. The y position is fixed at the centre point of the ellipse. Figure b: similarly, the traction along a line parallel to the y axis is visualized. The black bar is a representation of the ellipse along the corresponding axes. Note that centre of both orbits are re-centred around zero.

We expect the traction on the surface to be largest in the part of the trajectory where the bead approaches the wall closely. This feature is properly captured by the minimal model, as can be seen in the figure above. We compare the traction generated by the minimal model to the advanced model. We immediately notice that the peak values in both models occur at the edge of the elliptic trajectories. Here, the difference between the two models varies from $\sim 5\%$ (figure 18a, left side of the elliptic projection) to a maximum of $\sim 42\%$ (figure 18b, right side of the elliptic projection). Analyzing the traction further away from the cilium (~ 4 cilium lengths) these differences increase to 40% and 80%, respectively.

The difference in generated traction is relatively big compared to the difference in fluid velocity. This can by explained by the fact that in the advanced model more beads move closer to the surface. These beads near the cell wall have the biggest influence on the generated traction, in contrast to the fluid velocity where the beads far away from the cell surface are most important. However, the general trend in decay is similar in both models. Therefore, the minimal model can be used to gain semi-quantitative insight into the traction forces acting on the surface of the node.

6 Results - Synchronization in a system of two cilia

In this section we will present the results obtained from analyzing a minimal model consisting of two beads that represent two beating cilia. We will first analyze two beads moving on identical trajectories. In this system we observe synchronization, meaning the beads obtain the same phase variable ϕ. We continue by analyzing a system of two bead moving on non-identical trajectories. Here, no synchronization is observed.

6.1 Identical trajectories

We consider a system of two identical cilia with major and minor axes $A = 37.69$ and $B = 35.27$. Both cilia are given the same tilt using the rotations: $\mathcal{R}_x(0.175\pi)$, $\mathcal{R}_y(0.075\pi)$ and $\mathcal{R}_z(0.05\pi)$. We place the centre of cilia 1 and 2 respectively at $\mathbf{r}_1^c = (3.55, 10.00, 28.83)$ and $\mathbf{r}_2^c = (3.39, 110.00, 28.83)$, resulting in a distance of separation $d = 100$, or roughly two cilium lengths. The cilia are given an initial phase difference of $\pi/3$. A visual representation is given in figure 19.

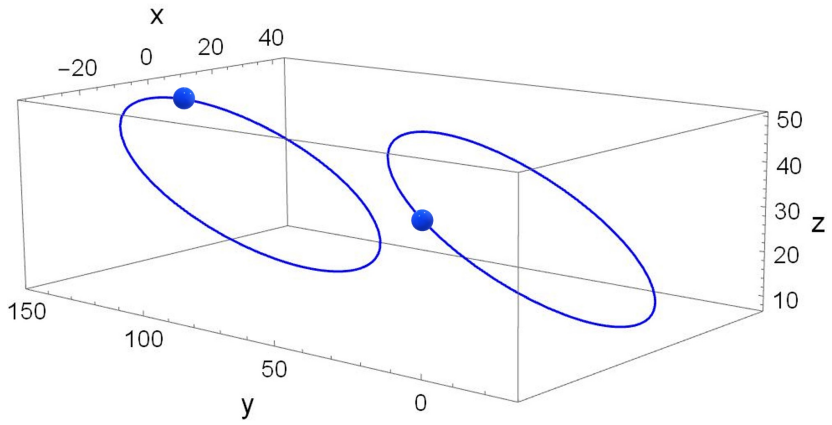

Figure 19: A system of two cilia that start beating with a phase difference of $\pi/3$ The centre of both ellipses are placed at $z = 28.87$ and separated by two cilium lengths.

Solving equation 47 reveals the dynamics of our coupled system of two cilia. We obtain phase variable ϕ_1 and ϕ_2 and consequently obtain the position of the beads: $\mathbf{r}_1(t)$ and $\mathbf{r}_2(t)$. We define the reduced position vector $\mathbf{r}_1^*(t) = \mathbf{r}_1(t) - \mathbf{r}_1^c$ and $\mathbf{r}_2^*(t) = \mathbf{r}_2(t) - \mathbf{r}_2^c$. Finally, we define the difference between the two as: $\Delta\mathbf{r}^*(t) = \mathbf{r}_1^*(t) - \mathbf{r}_2^*(t)$. These quantities are reported below during the first bead cycle:

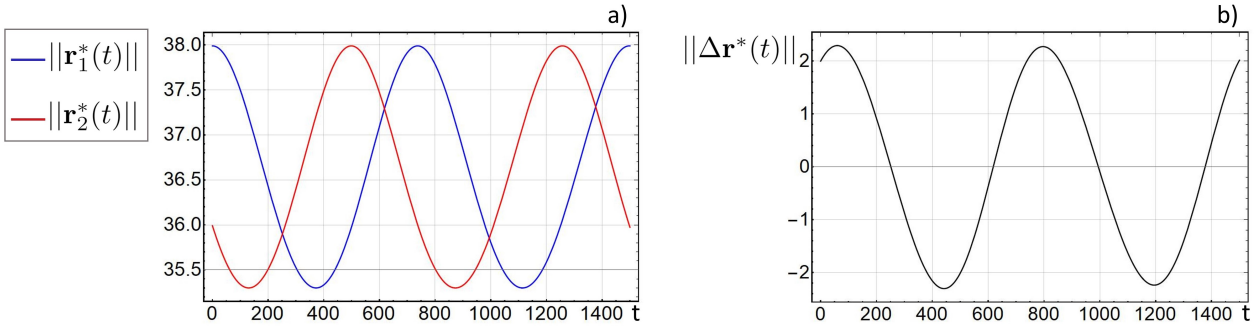

Figure 20: Figure a: The reduced position vectors of bead 1 and 2 are visualised in blue and red respectively. The two beads are given an initial phase difference of $\pi/3$. Figure b: The norm of the difference of the two position vectors is visualized during one period.

We continue by examining this system at various cilium separation lengths d during 4×10^6 times steps (contain roughly 2700 bead cycles). In figure 21 we report the difference in position of the two beads: $\Delta \mathbf{r}^*(t)$. We examine the system with inter-cilia spacing of $d = 50$, $d = 100$ and $d = 150$. We report the maximum difference in red, blue and green, respectively. We observe synchronization, meaning the difference in $\Delta \mathbf{r}^*(t)$ approaches zero when we increase the number of bead cycles.

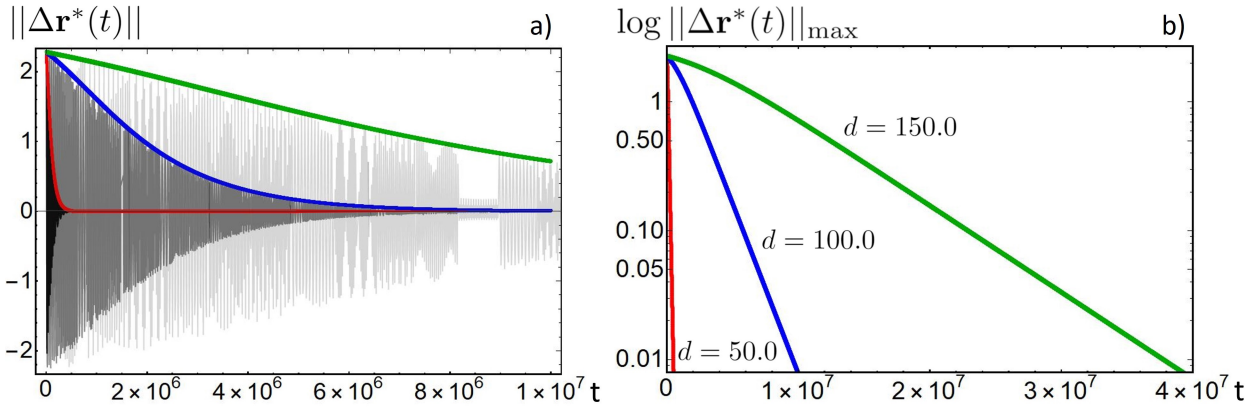

Figure 21: Figure a: The difference in position between two beads during ~ 2700 bead cycles. The colored lines indicate the maximum difference observed between two beads. The three different cilia spacing of $d = 50$, $d = 100$ and $d = 150$ are presented in red, blue and green, respectively. The gaps that seem to appear in the data are visualization affects rather than computational effects. Figure b: The maximum difference between the two beads in the three different systems are presented.

Above, we observe that hydrodynamic coupling synchronizes a system of two moving beads fixed on identical elliptic trajectories. The rate in which synchronization occurs depends on the inter-cilia spacing; if the spacing is larger synchronization takes longer. We compute the decay values of the three system with various inter-cilia spacing and observed decay values of -1.17×10^{-5}, -5.90×10^{-7} and -1.50×10^{-7}, corresponding to the red, blue and green line of figure 21, respectively. No explicit relation between inter-cilia spacing and synchronization time is observed yet. In order to further investigate this more data should be obtained. If the cilia spacing is of the order of 1 cilium length synchronization occurs after $\sim 0.5 \times 10^6$ times steps (about half a minute in real time), containing roughly 330 bead cycles. We continue to investigate a system where two beads move on slightly non-identical trajectories.

6.2 Non-identical trajectories

We consider a system of two non-identical cilia. The specific features of this system are acquired by analyzing data provided by Perugachi Israels, using the methodology of section 4. Thereby we acquire the elliptic trajectory of bead 1 and 2. We obtain values for the major and minor axes of bead 1 and 2: $A_1 = 37.99$, $B_1 = 35.30$, $A_2 = 34.23$ and $B_1 = 32.85$. The position of the centre of the trajectory of cilium 1 and 2 are obtained: $\mathbf{r}_1^c = (3.55, -12.48, 30.17)$ and $\mathbf{r}_2^c = (3.39, 66.34, 32.26)$. This results in a distance of separation $d = 78.8$. Both cilia are tilted similarly using the rotations: $\mathcal{R}_x(0.2\pi)$, $\mathcal{R}_y(0.0\pi)$ and $\mathcal{R}_z(0.125\pi)$. The cilia are given an initial phase difference of $\pi/3$.

Solving equation 47 reveals the dynamics of our system of two cilia. We obtain phase variables ϕ_1 and ϕ_2. Using these we obtain the position of the beads: $\mathbf{r}_1(t)$ and $\mathbf{r}_2(t)$. Analogous to section 6.1 we define the reduced position vector $\mathbf{r}_1^*(t) = \mathbf{r}_1(t) - \mathbf{r}_1^c$ and $\mathbf{r}_2^*(t) = \mathbf{r}_2(t) - \mathbf{r}_2^c$. Finally, we define the difference between the two as: $\Delta\mathbf{r}^*(t) = \mathbf{r}_1^*(t) - \mathbf{r}_2^*(t)$. The norm of these quantities are reported below during the first ten bead cycle:

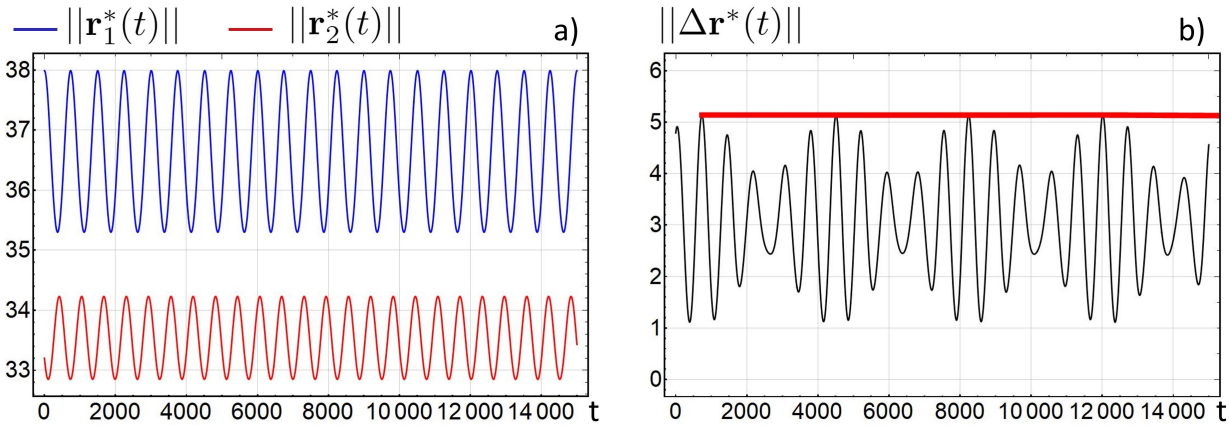

Figure 22: Figure a: The (reduced) position of bead 1 and 2 are visualized in blue en red respectively. Figure b: The difference in position between the two beads is presented. The red line denotes the maximum difference. We examine the system during ten bead cycles.

We continue by examining the system during 4×10^6 time steps, containing roughly 2700 bead cycles. The maximum difference as reported in figure 22b does not change when examining the system at any later time. This means the two beads in this system do not synchronize.

7 Discussion

The minimal model provided in this thesis may help understand the role cilia play in breaking the left-right symmetry during embryonic development. In this section we discuss the differences and similarities between the minimal model and the advanced model. We also consider whether the minimal model is sufficiently accurate to study processes in the node like the flow-induced movement of small signaling molecules.

In section 5 the minimal model and the advanced model are compared. We compared only net quantities (net fluid velocity and net traction), which is justified by the results presented in figure 12 and 17. Based on the results presented in section 5 we conclude that only when examining the flow field $\sim 3\,\mu$m above the surface the minimal model of a cilium mimics the flow profile of advanced model rather well. In the direction where most of the fluid movement is generated (perpendicular to the direction of the motion of the bead) the two models correspond best. Moreover, the trend of the (power-law) decay of the fluid velocity as a function of the distance behaves similarly in both models. Therefore, we conclude that the minimal model can be used to obtain semi-quantitative insight into the generated flow field in the plane of the centre of the ellipse. This is the most relevant part of the flow field as it is considerably larger than the flow in the plane above the cilium. When comparing the generated traction forces between the two models the difference (compared to the fluid velocity) is more pronounced. However, the general trend in decay is similar in both models and the minimal model captures the expected features as described in section 5. Therefore, the minimal model can also be used to gain semi-quantitative insight into the traction forces that act on the surface of the node.

In section 6 we studied synchronization in a system of two neighbouring cilia represented by spherical beads. As expected, we observed synchronization in a system where the beads move on identical trajectories. However, synchronization is not observed when studying a system where the two beads move on non-identical trajectories. The origin thereof can be traced to the minimal system exhibiting only one degree of freedom. The beads are driven by a constant force and move on a fixed trajectory. Consequently, completing synchronization is not possible. This problem can be solved by adding another degree of freedom to the model: the length of the major/minor axes and the orientation of the ellipse could be made variable.

The minimal model captures some general features that are observed in experimental research (see section 5 and 6). However, our minimal model differs form biological systems in a number of ways. In both the minimal and the more advanced model, the environment of the node is recreated by implementing a nearby boundary that represents the cell wall to which cilia are attached. The boundary in the model is flat, unlike the actual boundary in the node, which consists of many rounded shaped cells. The cells make up the bottom of the node, which is shaped like a triangular pit. Both these shapes are not accounted for in the model. We do expect these shapes to have a significant influence on the flow near the cell boundary. However, we expect this to have a much less pronounced effect on the flow further above the cell wall. This is based on the observation that the upper part of the cilium affects the flow in the node the most and determines its general direction.

In our model we only incorporated a single boundary representing the bottom of the node. However, the node is a cavity consisting of a bottom-, side- and top wall. In experimental research a counter flow is observed, caused by the presence of the additional walls in the node. In a study by Smith *et al.* (2011) a method is developed to model the upper membrane of the node [23]. In this mathematical model a counter flow in the upper region in the node is observed. The methodology by Smith *et al.* (2011) could be used to incorporate the upper membrane of the node in the minimal model.

8 Conclusion and outlook

In this thesis we have investigated the influence of a minimal model of a beating cilium, as originally proposed by Vilfan and Jülicher (2006) [1], on the surrounding fluid. The cilium was modeled as a spherical bead moving on a fixed elliptic trajectory above a nearby flat boundary, which mimics the shape of the node. The effect of the boundary on the flow is taken into account via the Blake tensor. We explored the influence of the bead on the surrounding substrate by analyzing the net traction forces that act on the cell surface and the net velocity of the fluid in the node. We compared these quantities to a more advanced model by Perugachi Israels [2]. In her model the full shape of the cilium is taken into account. By comparing the two models we were able to determine that, surprisingly, the minimal model semi-quantitatively captures the fluid dynamics and other properties of the advanced model. To be precise, the fluid velocity generated by the minimal model correspond best to the advanced model at $\sim 3\,\mu$m above the surface. In addition, the trend of the decay of the fluid velocity as a function of the distance behaves similarly in both models. However, when comparing the fluid flow above the tip of the cilium we observe a sizeable difference between the two models. Here, the decay of the generated fluid velocities in both models do not follow the same trend and the minimal model generates far less fluid motion compared to the advanced model. Nevertheless, this direction is less relevant to our modeling as the flow perpendicular and far above the cell surface is much smaller compared to the flow parallel to the surface (in the plane of the cilium tip).

Next, we compared the minimal model to biological reality. The minimal model was indeed found to generate a flow directed from left to right. The observed fluid velocity is of the same order of magnitude as experimentally observed values. This, and our other results, gives us confidence in the minimal model. Therefore, we conclude that it can be used to qualitatively study nodal processes like the flow-induced movement of small signaling molecules. Studying these nodal processes may contribute to determining how nodal flow exactly lead to asymmetric gen expression.

Duplicating the minimal model allowed us to study synchronization between neighbouring cilia. The effect that neighboring cilia have on each other is taken into account using Faxén's law. As expected, hydrodynamic coupling resulted in synchronization between neighbouring beads in the minimal model. The rate at which synchronization occurs depends on the inter-cilia spacing; if the spacing is larger synchronization takes longer. However, when examining two beads on slightly non-identical trajectories no synchronization is observed. This problem can be solved by adding another degree of freedom to the model: the length of the major/minor axes and the orientation of the ellipse could be made variable. Altering the minimal model is left for future study.

References

[1] Andrej Vilfan and Frank Jülicher. Hydrodynamic flow patterns and synchronization of beating cilia. *Physical review letters*, **96**(5):058102, 2006.

[2] Cintia Perugachi Israels. Cilia-induced flow in the embryonic node of mice and asymmetric gene expression. *Batcholor Thesis, Natuur- en Sterrenkunde, Universiteit Utrecht*, 2020.

[3] Nobutaka Hirokawa, Yasushi Okada, and Yosuke Tanaka. Fluid dynamic mechanism responsible for breaking the left-right symmetry of the human body: the nodal flow. *Annual review of fluid mechanics*, **41**:53–72, 2009.

[4] Petra Pennekamp, Tabea Menchen, Bernd Dworniczak, and Hiroshi Hamada. Situs inversus and ciliary abnormalities: 20 years later, what is the connection? *Cilia*, **4**(1):1, 2015.

[5] Yasushi Okada, Shigenori Nonaka, Yosuke Tanaka, Yukio Saijoh, Hiroshi Hamada, and Nobutaka Hirokawa. Abnormal nodal flow precedes situs inversus in iv and inv mice. *Molecular cell*, **4**(4):459–468, 1999.

[6] Kyosuke Shinohara, Aiko Kawasumi, Atsuko Takamatsu, Satoko Yoshiba, Yanick Botilde, Noboru Motoyama, Walter Reith, Bénédicte Durand, Hidetaka Shiratori, and Hiroshi Hamada. Two rotating cilia in the node cavity are sufficient to break left–right symmetry in the mouse embryo. *Nature communications*, **3**(1):1–8, 2012.

[7] Yasushi Okada, Sen Takeda, Yosuke Tanaka, Juan-Carlos Izpisúa Belmonte, and Nobutaka Hirokawa. Mechanism of nodal flow: a conserved symmetry breaking event in left-right axis determination. *Cell*, **121**(4):633–644, 2005.

[8] Shigenori Nonaka, Hidetaka Shiratori, Yukio Saijoh, and Hiroshi Hamada. Determination of left–right patterning of the mouse embryo by artificial nodal flow. *Nature*, **418**(6893):96–99, 2002.

[9] Shay Gueron and Konstantin Levit-Gurevich. Energetic considerations of ciliary beating and the advantage of metachronal coordination. *Proceedings of the National Academy of Sciences*, **96**(22):12240–12245, 1999.

[10] SN Khaderi, JMJ Den Toonder, and PR Onck. Microfluidic propulsion by the metachronal beating of magnetic artificial cilia: a numerical analysis. *Journal of fluid mechanics*, **688**:44–65, 2011.

[11] Shay Gueron, Konstantin Levit-Gurevich, Nadav Liron, and Jacob J Blum. Cilia internal mechanism and metachronal coordination as the result of hydrodynamical coupling. *Proceedings of the National Academy of Sciences*, **94**(12):6001–6006, 1997.

[12] R Di Leonardo, András Búzás, Lóránd Kelemen, Gaszton Vizsnyiczai, László Oroszi, and Pál Ormos. Hydrodynamic synchronization of light driven microrotors. *Physical review letters*, **109**(3):034104, 2012.

[13] Douglas R Brumley, Kirsty Y Wan, Marco Polin, and Raymond E Goldstein. Flagellar synchronization through direct hydrodynamic interactions. *Elife*, **3**:e02750, 2014.

[14] Aref Ghorbani and Ali Najafi. Symplectic and antiplectic waves in an array of beating cilia attached to a closed body. *Physical Review E*, **95**(5):052412, 2017.

[15] Christopher Brennen and Howard Winet. Fluid mechanics of propulsion by cilia and flagella. *Annual Review of Fluid Mechanics*, **9**(1):339–398, 1977.

[16] Anneloes Dummer, Christian Poelma, Marco C DeRuiter, Marie-José TH Goumans, and Beerend P Hierck. Measuring the primary cilium length: improved method for unbiased high-throughput analysis. *Cilia*, **5**(1):7, 2016.

[17] BA Afzelius. Cilia-related diseases. *The Journal of Pathology: A Journal of the Pathological Society of Great Britain and Ireland*, **204**(4):470–477, 2004.

[18] Ingmar H Riedel-Kruse, Andreas Hilfinger, Jonathon Howard, and Frank Jülicher. How molecular motors shape the flagellar beat. *HFSP journal*, **1**(3):192–208, 2007.

[19] Javier Buceta, Marta Ibañes, Diego Rasskin-Gutman, Yasushi Okada, Nobutaka Hirokawa, and Juan Carlos Izpisúa-Belmonte. Nodal cilia dynamics and the specification of the left/right axis in early vertebrate embryo development. *Biophysical journal*, **89**(4):2199–2209, 2005.

[20] DJ Smith, EA Gaffney, and JR Blake. Discrete cilia modelling with singularity distributions: application to the embryonic node and the airway surface liquid. *Bulletin of mathematical biology*, **69**(5):1477–1510, 2007.

[21] John Blake. Hydrodynamic calculations on the movements of cilia and flagella i. paramecium. *Journal of theoretical biology*, **45**(1):183–203, 1974.

[22] Shigenori Nonaka, Satoko Yoshiba, Daisuke Watanabe, Shingo Ikeuchi, Tomonobu Goto, Wallace F Marshall, and Hiroshi Hamada. De novo formation of left–right asymmetry by posterior tilt of nodal cilia. *PLoS Biol*, **3**(8):e268, 2005.

[23] David J Smith, Andrew A Smith, and John R Blake. Mathematical embryology: the fluid mechanics of nodal cilia. *Journal of Engineering Mathematics*, **70**(1-3):255–279, 2011.

[24] Dominic P Norris. Cilia, calcium and the basis of left-right asymmetry. *BMC biology*, **10**(1):1–8, 2012.

[25] James McGrath, Stefan Somlo, Svetlana Makova, Xin Tian, and Martina Brueckner. Two populations of node monocilia initiate left-right asymmetry in the mouse. *Cell*, **114**(1):61–73, 2003.

[26] Larisa Gheber and Zvi Priel. Synchronization between beating cilia. *Biophysical journal*, 55(1):183–191, 1989.

[27] Joseph H. Spurk and Nuri Aksel. *Fluid Mechanics*, chapter 4; Equations of Motion for Particular Fluid. Springer, second edition, 2008.

[28] Joost de Graaf. *Advanced Topics in Theoretical Physics: The Microscopic Origin of Hydrodynamics*, chapter 2,5. Institute for Theoretical Physics, Utrecht University, 2019.

[29] John R. Taylor. *Classical Mechanics*, chapter 16; Continuum Mechanics. University Science Books, 2005.

[30] Christopher J Gordon. The mouse thermoregulatory system: Its impact on translating biomedical data to humans. *Physiology & behavior*, **179**:55–66, 2017.

[31] Maciej Lisicki. *Four approaches to hydrodynamic Green's functions–the Oseen tensors.* Institute of Theoretical Physics, University of Warsaw, arXiv preprint:1312.6231, 2013.

[32] Erik M Gauger, Matthew T Downton, and Holger Stark. Fluid transport at low reynolds number with magnetically actuated artificial cilia. *The European Physical Journal E*, **28**(2):231–242, 2009.

[33] Shay Gueron and Konstantin Levit-Gurevich. Computation of the internal forces in cilia: application to ciliary motion, the effects of viscosity, and cilia interactions. *Biophysical journal*, **74**(4):1658–1676, 1998.

[34] M. Hinczewski Y. von Hansen and R. R. Netz. Hydrodynamic screening near planar boundaries: Effects on semiflexible polymer dynamics. *The journal of chemical physics 134*, **4**:1, 2011.

[35] J.R. Blake. A note on the image system for a stokeslet in a no-slip boundary. *Cilia*, **4**(1):1, 1971.

[36] James Gray and GJ Hancock. The propulsion of sea-urchin spermatozoa. *Journal of Experimental Biology*, **32**(4):802–814, 1955.

[37] Douglas R Brumley, Marco Polin, Timothy J Pedley, and Raymond E Goldstein. Hydrodynamic synchronization and metachronal waves on the surface of the colonial alga volvox carteri. *Physical review letters*, **109**(26):268102, 2012.